A high-resolution Godunov method for compressible multi-material flow on overlapping grids

J.W. Banks [1], D.W. Schwendeman [2], and A.K. Kapila [3]

Department of Mathematical Sciences, Rensselaer Polytechnic Institute, Troy, New York, 12180

and W.D. Henshaw [4]

Center for Applied Scientific Computing, Lawrence Livermore National Lab, Livermore, California, 94551

Abstract

A numerical method is described for inviscid, compressible, multi-material flow in two space dimensions. The flow is governed by the multi-material Euler equations with a general mixture equation of state. Composite overlapping grids are used to handle complex flow geometry and block-structured adaptive mesh refinement (AMR) is used to locally increase grid resolution near shocks and material interfaces. The discretization of the governing equations is based on a high-resolution Godunov method, but includes an energy correction designed to suppress numerical errors that develop near a material interface for standard, conservative shock-capturing schemes. The energy correction is constructed based on a uniform pressure-velocity flow and is significant only near the captured interface. A variety of two-material flows are presented to verify the accuracy of the numerical approach and to illustrate its use. These flows assume an equation of state for the mixture based on the Jones-Wilkins-Lee (JWL) forms for the components. This equation of state includes a mixture of ideal gases as a special case. Flow problems considered include unsteady one-dimensional shock-interface collision, steady interaction of an planar interface and an oblique shock, planar shock interaction with a collection of gas-filled cylindrical inhomogeneities, and the impulsive motion of the two-component mixture in a rigid cylindrical vessel.

Key words: Euler equations, compressible flow, Godunov methods, overlapping grids, multi-material flows.

1 Introduction

Compressible multi-material flows arise in many areas of science and engineering. Problems of interest typically involve material interfaces separating regions of pure constituents. The geometry of such problems can be comparatively simple as in the case of an isolated bubble suspended in a flow, or complex as in the case of heterogeneous granular solids. In either case, the material interface is a prominent feature of the flow and its numerical treatment must be performed in a physically consistent manner. For high-speed compressible flows governed by a multi-material version of the Euler equations, it is well known that standard conservative shock-capturing schemes produce unphysical numerical oscillations near the material interface, the cause of the error being the calculation of pressure based on conservative cell-averaged variables. Within the context of shock capturing methods, the difficulty has been addressed by a number of investigators. For example, beginning with [1,2], Karni developed an interface-capturing method based on the primitive form of the governing equations. In this approach, the numerical treatment of pressure is handled accurately near the interface, but the method is not conservative. However, a correction can be constructed so that the method is locally conservative near shocks [3]. Other shock-capturing methods are based on conservative formulations of the equations and rely on various special discretizations near material interfaces. In [4], for example, Abgrall introduced a method with a special discretization of the advection equation for the species mass fraction designed to suppress numerical oscillations near the interface. This approach was modified in [5] for advection equations associated with certain parameters of the constituent equations of state (such as the ratio of specific heats for an ideal gas). Finally, in [6], a correction to the total energy was devised to eliminate unphysical behavior.

Other numerical approaches to handle multi-material flows have been developed based on interface tracking. Such methods include, for example, the ghost-fluid method (GFM), arbitrary-Lagrangian-Eulerian (ALE) methods, and volume-of-fluid (volume-tracking) methods. The essential feature of these methods is the introduction of an explicit description for the material interface. This explicit description elliminates the unphysical behavior seen in capturing methods but at the cost of performing the interface reconstruction. In the GFM [7–9] a function is introduced whose zero level set represents the material interface. The governing equations for each constituent are solved on either side of the interface with the aid of "ghost-fluid" points which are constructed across the interface. ALE methods [10,11] advect the material interface and use boundary-conforming grids for their discretization. Finally, the volume-of-fluid methods [12,13] reconstruct a material interface from advected volume fractions at every step and thus maintain sharp interfaces. This is by no means a comprehensive list of methods for multi-material flow solvers, but rather, just a sampling. A more comprehensive overview of methods for multi-material problems is provided in [14].

[1] Graduate research support was given by NSF under grants DMS-9983646 and DMS-0312040, and by the Office of Science, U.S. Department of Energy, through summer visits to the Lawrence Livermore National Laboratory.

[2] Research support was given by NSF under grant DMS-0312040 and by Lawrence Livermore National Laboratory under subcontracts B537580 and B548468.

[3] Research support was given by NSF under grant DMS-0312040.

[4] Research supported was given under the auspices of the U.S. Department of Energy by the University of California, Lawrence Livermore National Laboratory under contract No.W-7405-Eng-48.

This paper considers two-material flows as described by the multi-material Euler equations. The equations include an indicator function which measures the mass fraction of one of the species and thus determines the state of the mixture. A general equation of state is introduced for each constituent, and these are used to construct an equation of state for the mixture based on certain closure conditions. A numerical method is developed based on the conservative form of the equations. The method is a high-resolution extension of Godunov's method [15] and includes a correction of the discretization of the energy equation designed to suppress numerical oscillations that would occur near a sharp material interface. The energy correction, based on an analysis of a uniform-pressure-velocity flow, is applied at the level of the truncation error and is active only near material interfaces. The numerical method is similar in spirit to those developed in [4] and [5], but it differs from previous works in that it may be applied to any equation of state for the mixture. In addition, discretization of the equations is carried out using composite overlapping grids in order to handle complex flow geometries [16] and includes block-structured adaptive mesh refinement (AMR) in order to represent sharp features of the flow (such as the material interface and shocks) with numerical efficiency [17]. This aspect of the method builds on the work in [18] for the numerical treatment of the reactive Euler equations on overlapping grids.

An important new aspect of the present work is to show how a standard shock-capturing method, such as Godunov's method, can be modified to effectively and efficiently compute multi-material flows in complex geometries. In addition, the method is not restricted to mixture equations of state based on ideal equations of state (or similar forms) for the constituents. For example, the constituent equations of state discussed in this paper are based on Jones-Wilkins-Lee (JWL) forms which are Mie-Grüneisen-type equations of state [19]. This choice is made with the application of condensed-phase, high-energy explosives in mind, although the present study focuses on inert flows only. An extension of the numerical approach to multi-material reactive flow is in progress.

The subsequent sections of the paper begin with a discussion of the governing equations in Section 2. This is followed in Section 3 by a study of a specific one-dimensional Riemann problem involving a simple material contact where difficulties with standard shock-capturing schemes are revealed. These difficulties are illustrated using Godunov's method with an exact Riemann solver and this provides a motivation for the energy correction designed to eliminate the numerical errors for this case. We introduce our full numerical method in Section 4. Here, we begin with a brief discussion of the various elements of the numerical approach needed to handle overlapping grids with AMR (the full details are given in [18]) but then focus our attention on the new aspects of the numerical method. This includes the treatment of the second-order slope-correction in primitive variables, the Roe Riemann solver for a general mixture equation of state, and the energy correction for this Riemann solver. We also include a discussion of the numerical treatment of the mixture equation of state, which is defined implicitly for the general case.

The numerical method is used to solve a number of multi-material flows and these are presented in Section 5. The first problems discussed are used to study the behavior and accuracy of the method. For example, we use the method of analytic solutions to demonstrate second-order convergence of the method for smooth flows using both a single Cartesian grid and an overlapping grid consisting of two component grids. A one-dimensional problem involving the interaction of a shock and a material interface is studied in order to assess the behavior of the energy-corrected scheme for non-smooth flows. Here, we compare the numerical solution with the exact solution and find excellent agreement. As a further test of the numerical method we compute the solution of a two-dimensional flow involving the steady interaction of a planar interface and an oblique shock. The exact solution

for this flow is determined based on a shock-polar analysis and this solution is used to assess the accuracy of the method. Overall we find excellent agreement with the exact solution for this two-dimensional flow. Finally, we show results for more complex flows in which exact solutions are not available. These include the interaction of a planar shock with a collection of gas bubbles and the impulsive motion of a two-component mixture within a rigid cylindrical vessel. In the latter problem, we also examine the grid convergence of the full method using AMR, the behavior of the grid overlap on the numerical solution, and the Richtmyer-Meshkov instability that develops near the interface.

2 Governing Equations

We consider a mixture of two inviscid, compressible materials, and assume that in two dimensions the density ρ, velocities (u_1, u_2), pressure p, and total energy E of the mixture satisfy the usual balance equations,

$$\frac{\partial}{\partial t}\begin{bmatrix}\rho\\ \rho u_1\\ \rho u_2\\ E\end{bmatrix} + \frac{\partial}{\partial x_1}\begin{bmatrix}\rho u_1\\ \rho {u_1}^2 + p\\ \rho u_1 u_2\\ u_1(E+p)\end{bmatrix} + \frac{\partial}{\partial x_2}\begin{bmatrix}\rho u_2\\ \rho u_1 u_2\\ \rho {u_2}^2 + p\\ u_2(E+p)\end{bmatrix} = 0, \tag{1}$$

representing conservation of mass, momentum and energy for the mixture. The composition of the mixture is determined by the mass fraction ϕ_a of fluid a and the mass fraction $\phi_b = 1 - \phi_a$ of fluid b. We assume that the materials are chemically inert so that ϕ_a satisfies

$$\frac{\partial \phi_a}{\partial t} + u_1 \frac{\partial \phi_a}{\partial x_1} + u_2 \frac{\partial \phi_a}{\partial x_2} = 0. \tag{2}$$

(A similar equation holds for ϕ_b assuming that both constituents move with the mixture velocity.) The advection equation for ϕ_a may be combined with the balance equations in (1) to give the following conservation equations governing the two-material mixture:

$$\frac{\partial}{\partial t}\mathbf{u} + \frac{\partial}{\partial x_1}\mathbf{f}_1(\mathbf{u}) + \frac{\partial}{\partial x_2}\mathbf{f}_2(\mathbf{u}) = 0, \tag{3}$$

where

$$\mathbf{u} = \begin{bmatrix}\rho\\ \rho u_1\\ \rho u_2\\ E\\ \rho\phi_a\end{bmatrix}, \qquad \mathbf{f}_1(\mathbf{u}) = \begin{bmatrix}\rho u_1\\ \rho {u_1}^2 + p\\ \rho u_1 u_2\\ u_1(E+p)\\ \rho u_1 \phi_a\end{bmatrix}, \qquad \mathbf{f}_2(\mathbf{u}) = \begin{bmatrix}\rho u_2\\ \rho u_1 u_2\\ \rho {u_2}^2 + p\\ u_2(E+p)\\ \rho u_2 \phi_a\end{bmatrix}.$$

The total energy for the mixture is given by

$$E = \rho e + \frac{1}{2}\rho\left({u_1}^2 + {u_2}^2\right),$$

where $e = e(\rho, p, \phi_a)$ is the specific internal energy, which is specified by an equation of state for the mixture. It is assumed that the equations have been rendered dimensionless using suitable scalings of the variables.

In order to construct an equation of state for the mixture, we first describe the mechanical and thermal properties of the pure constituents. For our applications of interest, we assume the pure materials are governed by mechanical and thermal equations of state of Jones-Wilkins-Lee (JWL) form, namely

$$e_k = \frac{p_k v_k}{\omega_k} - \mathcal{F}_k(v_k) + \mathcal{F}_k(v_{0,k}), \qquad p_k = \frac{\omega_k}{v_k}\left(C_{v,k}T_k + \mathcal{Z}_k(v_k) - \mathcal{Z}_k(v_{0,k})\right), \tag{4}$$

where v_k, p_k, e_k and T_k are the specific volume, pressure, specific energy and temperature, respectively, for material k, $k = a, b$, and $v_{0,k}$ is a reference specific volume. The JWL forms are special cases of Mie-Grüneisen equations of state, and are often used in models of condensed-phase explosives [19], an application that motivates our work. In the JWL forms, ω_k is the Grüneisen constant, $C_{v,k}$ is the specific heat at constant volume (assumed constant for each k), and $\mathcal{F}_k$ and $\mathcal{Z}_k$ are stiffening functions, which are given by

$$\mathcal{F}_k(v_k) = A_k\left(\frac{v_k}{\omega_k} - \frac{1}{R_{1,k}}\right)\exp(-R_{1,k}v_k) + B_k\left(\frac{v_k}{\omega_k} - \frac{1}{R_{2,k}}\right)\exp(-R_{2,k}v_k), \tag{5}$$

and

$$\mathcal{Z}_k(v_k) = A_k\left(\frac{v_k}{\omega_k}\right)\exp(-R_{1,k}v_k) + B_k\left(\frac{v_k}{\omega_k}\right)\exp(-R_{2,k}v_k), \tag{6}$$

where A_k, B_k, $R_{1,k}$, $R_{2,k}$ are constants. The stiffening functions are fit to experimental data and the constants in (5) and (6) are available for a large number of materials at various conditions [20]. We note that the JWL forms in (4) also include the ideal gas case when $\mathcal{F}_a = \mathcal{F}_b = \mathcal{Z}_a = \mathcal{Z}_b = 0$. The mixture rules

$$e = \phi_a e_a + \phi_b e_b, \qquad v = \phi_a v_a + \phi_b v_b, \tag{7}$$

relate the specific energy, e, and the specific volume, $v = 1/\rho$, for the mixture in terms of the corresponding quantities of the material constituents. Following the work in [21–23], we assume pressure and temperature equilibrium so that $p = p_a = p_b$ and $T_a = T_b$, although other closure conditions may be more appropriate for other applications. The closure conditions provide the final equations needed to specify (implicitly) an equation of state for the mixture.

For example, in the special case of an ideal gas, the mechanical and thermal equations of state in (4) reduce to

$$e_k = C_{v,k} T_k = \frac{p_k v_k}{\gamma_k - 1}, \qquad \gamma_k = \omega_k + 1, \qquad k = a \text{ or } b. \tag{8}$$

These equations may be combined with the mixture rules in (7) and the closure conditions to give a mixture equation of state which takes the familiar form

$$e = \frac{p}{(\gamma - 1)\rho}, \tag{9}$$

but with an effective ratio of specific heats for the mixture given by

$$\gamma = \gamma(\phi_a) = \frac{\phi_a \gamma_a C_{v,a} + (1 - \phi_a)\, \gamma_b C_{v,b}}{\phi_a C_{v,a} + (1 - \phi_a)\, C_{v,b}}. \tag{10}$$

While our main focus is in flows for which a sharp interface separates regions with $\phi_a = 0$ from regions with $\phi_a = 1$, the governing equations with JWL equations of state for the constituents and physically-based mixture rules apply for flows with smooth mixture regions as well (as would be the case for an extension to reactive flows). For the case of a sharp interface, the governing equations in (3) for the mixture reduce to the usual Euler equations for the individual constituents on either side of the interface with the appropriate equation of state, either $k = a$ or b, given in (4). A numerical description of such flows, however, in which the material interface is captured requires a description for the mixture such as the one given above. Typically, the mixture region near the interface is narrow, spanning a few grid cells, and this is where the mixture rules apply. However, it is this narrow region that may cause numerical difficulties as we discuss in more detail in the next section.

3 A Shock-Capturing Method with Energy Correction

In this section, we describe a modification of a typical shock capturing scheme for the two-material equations. The modification involves an energy correction designed to suppress numerical errors that develop from the smeared interface between the materials. The purpose of this discussion is to introduce the basic numerical approach in a simple context before describing the full implementation in Section 4 below. Accordingly, we consider one-dimensional flow for which (3) reduces to

$$\frac{\partial}{\partial t}\mathbf{u} + \frac{\partial}{\partial x}\mathbf{f}(\mathbf{u}) = 0, \tag{11}$$

where

$$\mathbf{u} = \begin{bmatrix} \rho \\ \rho u \\ E \\ \rho\phi_a \end{bmatrix}, \qquad \mathbf{f}(\mathbf{u}) = \begin{bmatrix} \rho u \\ \rho u^2 + p \\ u(E+p) \\ \rho u \phi_a \end{bmatrix},$$

and assume an equation of state for the mixture given by (9) and (10). Let us define a uniform grid, $x_j = j\Delta x$, with cell average

$$U_j^n = \frac{1}{\Delta x} \int_{x_{j-1/2}}^{x_{j+1/2}} \mathbf{u}(x, t_n)\, dx. \tag{12}$$

A conservative discretization is

$$U_j^{n+1} = U_j^n - \frac{\Delta t}{\Delta x} \left(\mathbf{F}\left(U_j^n, U_{j+1}^n\right) - \mathbf{F}\left(U_{j-1}^n, U_j^n\right) \right) \tag{13}$$

where $\mathbf{F}(\mathbf{u}_L, \mathbf{u}_R)$ is a first-order numerical flux function associated with $\mathbf{f}$, such as the Godunov flux, and Δt is the time step.

An example of the numerical error that arises from the smeared interface between two materials is illustrated in Figure 1. The plots show the solution of (11) for the initial state given by $(\rho, u, p, \phi_a) = (0.138, 0.5, 1.0, 1.0)$ for $x < 0.4$ and $(1.0, 0.5, 1.0, 0.0)$ for $x \geq 0.4$. The interface, initially at $x = 0.4$, separates material a, an ideal gas with $\gamma_a = 1.67$ and $C_{v,a} = 3.11$, on the left from material b, an ideal gas with $\gamma_b = 1.4$ and $C_{v,b} = 0.72$, on the right. These values correspond to helium on the left and air on the right. The velocity and pressure are constant initially and remain constant in the exact solution for the flow, and thus the interface simply propagates to the right with velocity equal to 0.5. The black curve in each plot indicates this solution while the the red marks show the numerical solution given by (13) using the Godunov flux function and a grid with 250 cells in the interval $x \in [0, 1]$. Here, we observe that the numerical values for ρ and ϕ_a are in reasonably good agreement with the exact solution, but that the values for u and p are not. The smeared interface generates significant numerical errors in these latter two quantities that propagate away from the interface along the forward and backward characteristic waves, $u \pm c$, where c is the sound speed for the appropriate material state.

The numerical error shown in Figure 1 is typical for any standard conservative, shock-capturing scheme, such as Godunov's method, applied to (11). The error may be explained by considering one step in the numerical method from a *uniform-pressure-velocity* (UPV) state, as in the example above. Assuming that $u_j^n = V \geq 0$ and $p_j^n = P$ for all j at some time level t_n, Godunov's method becomes a simple upwind scheme

$$U_j^{n+1} = U_j^n - \frac{\Delta t}{\Delta x} \left(\mathbf{f}(U_j^n) - \mathbf{f}(U_{j-1}^n) \right), \tag{14}$$

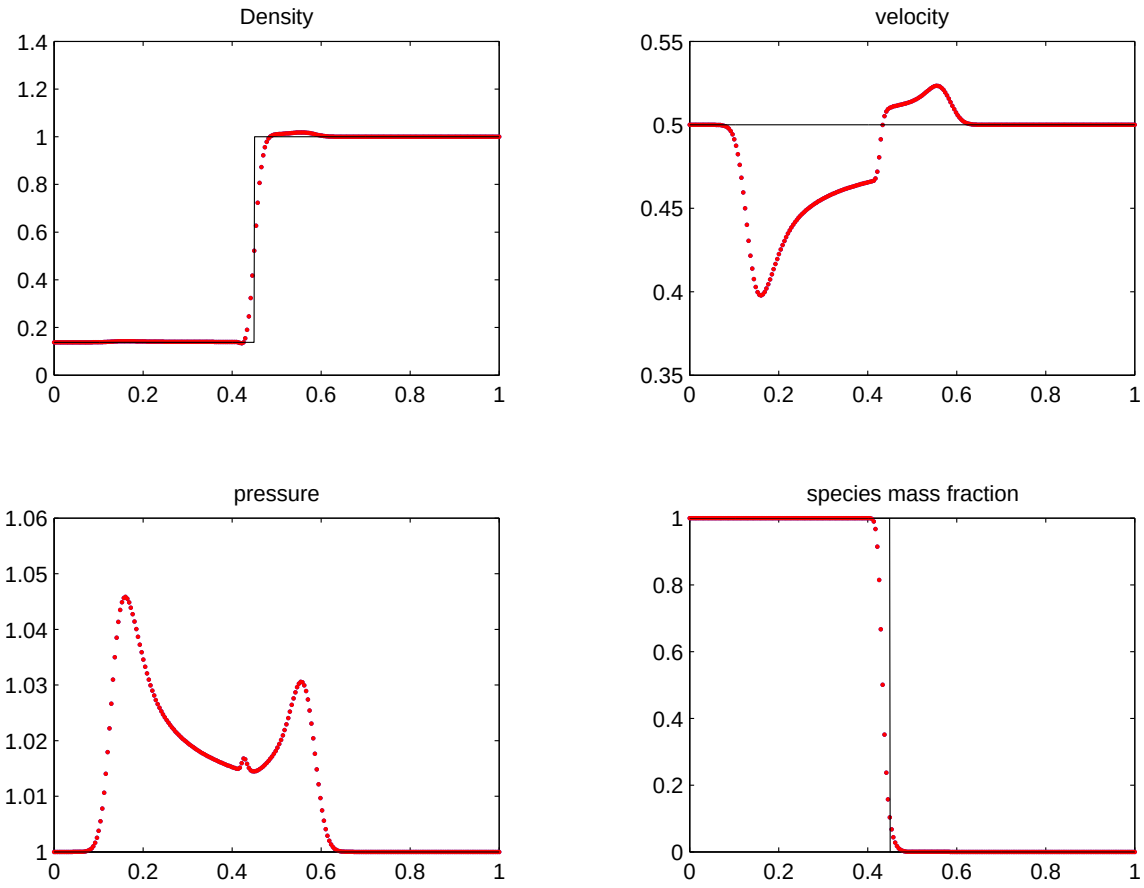

Fig. 1. Numerical solution at $t = 0.1$ using Godunov's method with $\Delta x = .004$ and CFL number equal to 0.8. The exact solution is shown by the black curves and the numerical solution is shown by the red marks.

from which we obtain

$$\rho_j^{n+1} = \rho_j^n - \frac{V\Delta t}{\Delta x}\left(\rho_j^n - \rho_{j-1}^n\right), \tag{15}$$

$$u_j^{n+1} = V, \tag{16}$$

$$\frac{p_j^{n+1}}{\gamma(\phi_{a,j}^{n+1}) - 1} = P\left\{\frac{1}{\gamma(\phi_{a,j}^n) - 1} - \frac{V\Delta t}{\Delta x}\left(\frac{1}{\gamma(\phi_{a,j}^n) - 1} - \frac{1}{\gamma(\phi_{a,j-1}^n) - 1}\right)\right\}, \tag{17}$$

$$\rho_j^{n+1}\phi_{a,j}^{n+1} = \rho_j^n\phi_{a,j}^n - \frac{V\Delta t}{\Delta x}\left(\rho_j^n\phi_{a,j}^n - \rho_{j-1}^n\phi_{a,j-1}^n\right). \tag{18}$$

From (15) and (18), we see that ρ and $\rho\phi_a$ evolve according to first-order upwind methods, and that u_j^{n+1} equals V after one time step according to (16). The difficulty arises in (17). Here, we note that p_j^{n+1} would equal P, and thus a UPV state would be maintained at t_{n+1}, if

$$\frac{1}{\gamma(\phi_{a,j}^{n+1}) - 1} = \frac{1}{\gamma(\phi_{a,j}^n) - 1} - \frac{V\Delta t}{\Delta x}\left(\frac{1}{\gamma(\phi_{a,j}^n) - 1} - \frac{1}{\gamma(\phi_{a,j-1}^n) - 1}\right), \tag{19}$$

which is a first-order upwind approximation of the equation

$$\frac{\partial \Gamma}{\partial t} + V\frac{\partial \Gamma}{\partial x} = 0, \qquad \Gamma \equiv \frac{1}{\gamma(\phi_a) - 1}. \tag{20}$$

Analytically, equation (20) holds (at least in some weak sense), since ϕ_a satisfies (2). However, the equality in (19) is *not* satisfied in general because this equation is not consistent with the discrete evolution equation for ϕ_a that can be derived from equations (15) and (18). It is this incompatibility which leads to the numerical error (after several time steps) of the type shown in Figure 1.

For the case of a mixture of ideal gases with equation of state given in (9) and (10), it is possible to remove the numerical error for UPV flow by deriving suitable difference approximations for ϕ_a. In the one-dimensional problem considered above, for example, UPV flow is maintained if (19) is used to advance ϕ_a instead of (18). This approach is in the spirit of the numerical method discussed in [4] and [5]. An advantage of this approach is that conservation of total mass, momentum and energy is maintained in the discrete equations (although conservation of the individual component materials is lost). However, the approach does not extend easily for the case of more general equations of state in which the EOS is defined implicitly, such as the JWL forms considered later in this paper.

An alternate numerical approach is based on (13) but incorporates an *energy correction* into the discretization. The correction is constructed to subtract the incompatibility error in the energy equation associated with the discretization of (20). An advantage of this approach is that it can handle general equations of state. For one-dimensional flow, the scheme has the quasi-conservative form

$$U_j^{n+1} = U_j^n - \frac{\Delta t}{\Delta x}\left(\mathbf{F}\left(U_j^n, U_{j+1}^n\right) - \mathbf{F}\left(U_{j-1}^n, U_j^n\right)\right) + \Delta G_j^{n+1}, \tag{21}$$

where $\Delta G_j^{n+1} = [0,\, 0,\, \Delta E_j^{n+1},\, 0]^T$ includes an energy correction given by

$$\Delta E_j^{n+1} = \frac{p_j^n - \tilde{p}_j^{n+1}}{\gamma(\phi_{a,j}^{n+1}) - 1}, \tag{22}$$

for the case of a mixture of ideal gases. (A suitable form for the energy correction for general equations of state is discussed in Section 4.2.2.) The value for $\tilde{p}_j^{n+1}$ in the formula for ΔE_j^{n+1} is the pressure in the conservative state $\tilde{U}_j^{n+1}$ computed in advance from

$$\tilde{U}_j^{n+1} = U_j^n - \frac{\Delta t}{\Delta x}\left(\mathbf{F}\left(U_j^n, \tilde{U}_{j+1}^n\right) - \mathbf{F}\left(\tilde{U}_{j-1}^n, U_j^n\right)\right), \tag{23}$$

where $\tilde{U}_{j-1}^n$ and $\tilde{U}_{j+1}^n$ are the conservative states corresponding to the primitive variables $(\rho_{j-1}^n,\, u_j^n,\, p_j^n,\, \phi_{a,j-1}^n)$ and $(\rho_{j+1}^n,\, u_j^n,\, p_j^n,\, \phi_{a,j+1}^n)$, respectively, i.e. a UPV state corresponding to U_j^n. The energy-corrected scheme now preserves uniform velocity and pressure in the numerical approximation of UPV flow for all time steps, and the previous numerical error associated with the smeared interface is suppressed as shown in Figure 2.

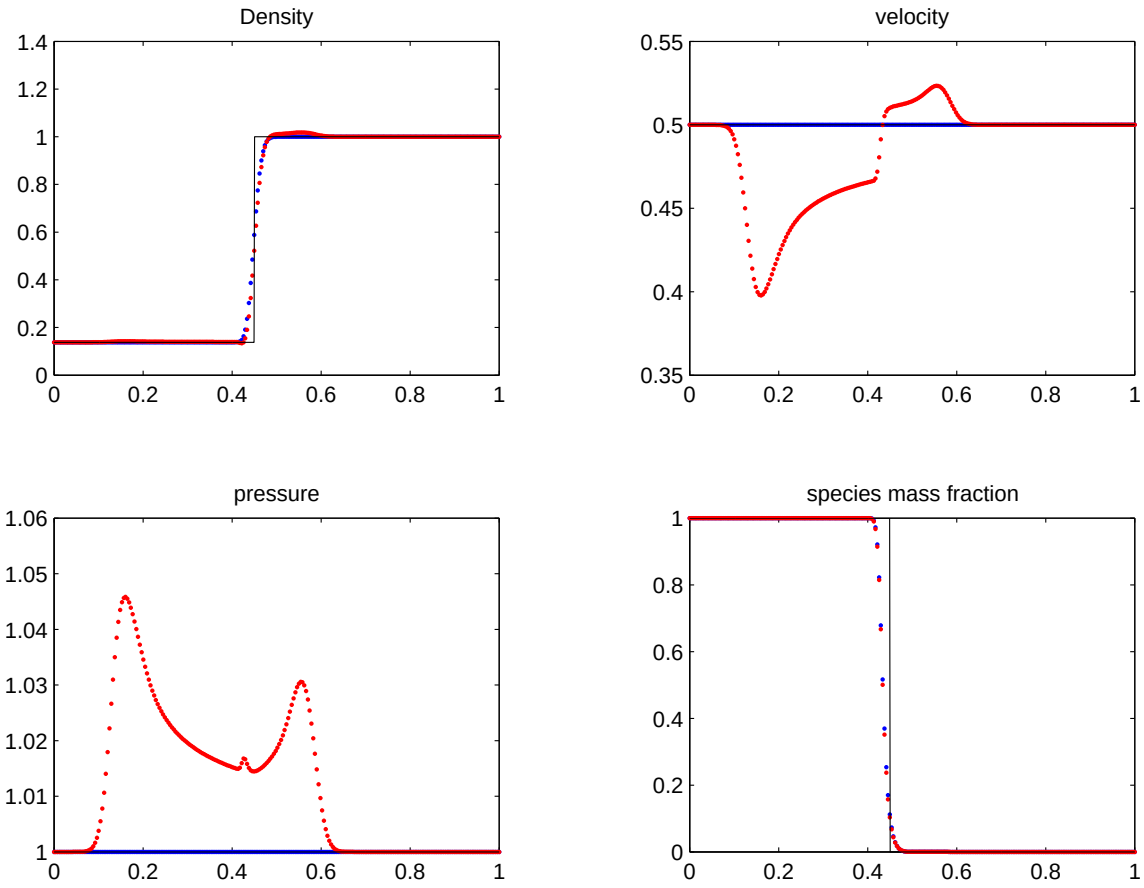

Fig. 2. Numerical solution at $t = 0.1$ using Godunov's method with $\Delta x = .004$ and CFL number 0.8. The exact solution is shown in black, Godunov's method without energy correction is shown in red, and Godunov's with energy correction is shown in blue.

A closer examination of the energy correction shows that its (leading-order) contribution to the truncation error, i.e. for $-\Delta E_j^{n+1}/\Delta t$, is given by

$$\tau_j^n = \Delta x|u|p\left(1 - \frac{|u|\Delta t}{\Delta x}\right)\left(\frac{\Gamma'}{\rho}\frac{\partial \rho}{\partial x} - \frac{\Gamma''}{2}\frac{\partial \phi_a}{\partial x}\right)\frac{\partial \phi_a}{\partial x}\bigg|_{x=x_j,\, t=t_n},$$

where $\Gamma = \Gamma(\phi_a)$ is defined in (20). Thus, the formal order of accuracy of the energy-corrected scheme in (21) is unchanged from the original Godunov method. Further, we note that the contribution to the truncation error depends on derivatives of ρ and ϕ_a so that its greatest effect occurs when ρ and ϕ_a vary rapidly and $u \neq 0$, such as near a moving material interface. (The energy correction is zero in regions where $u = 0$.) However, since the width of a captured moving interface increases gradually over time, the effect of the energy correction is expected to decrease. Away from the interface where the derivative of ϕ_a is approximately zero, the energy correction is negligible. In these regions of the flow, shock waves would be captured and evolve according to the usual conservative Godunov scheme. At isolated points in time and space it is possible for a material interface and a shock to collide. At such points, discrete conservation is not strictly maintained in the energy equation which is a possible concern (although mass and momentum are still conserved in the discrete equations). To address this issue, several problems involving shock-interface collisions

are studied numerically in Sections 5.2 and 5.3, and it is found that the energy-corrected scheme gives accurate results in terms of shock positions for such interactions. Hence, the energy correction has the desirable effect of suppressing numerical errors associated with the captured interface, while not adversely effecting the behavior of shocks in the flow.

Finally, we note that the computational cost associated with the calculation of ΔE_j^n is not large since the numerical flux calculations in (23) can be done inexpensively. This calculation depends on the choice of the particular numerical flux function. If, for example, the Godunov flux or approximate Roe flux function is chosen, then

$$\mathbf{F}\left(U_j^n, \tilde{U}_{j+1}^n\right) = \begin{cases} \mathbf{f}(U_j^n) & \text{if } u_j^n > 0 \\ \mathbf{f}(\tilde{U}_{j+1}^n) & \text{if } u_j^n < 0 \end{cases}$$

since U_j^n and $\tilde{U}_{j+1}^n$ belong to a UPV flow so that the jump across the acoustic fields is zero. A similar simplification applies for $\mathbf{F}\left(\tilde{U}_{j-1}^n, U_j^n\right)$.

4 A High-Resolution Method with Energy Correction

We now return to the governing equations in (3) for flow in two dimensions and describe a numerical discretization of the equations on composite overlapping grids with adaptive mesh refinement (AMR). Overlapping grids are used to handle complex flow geometries and AMR is used to handle fine-scale structures such as shocks and contacts (including the interface between fluids) with numerical efficiency. The basic numerical approach follows that described in [18], but includes several new modifications designed to handle multi-material flows. The basic overlapping grid framework, including AMR, is described in Section 4.1. Here we discuss a modification to the interpolation at the overlap between component grids and between grids at different refinement levels which is needed in order to maintain uniform-pressure-velocity (UPV) flow. A second-order, slope-limited extension of Godunov's method is employed on each curvilinear component grid in the overlapping-AMR grid system. This scheme, as described in Section 4.2, is written in a predictor-corrector fashion where the slope correction employed in the predictor step is modified to maintain UPV flow. A Roe Riemann solver is used to compute numerical fluxes in the corrector step, and this also requires an extension to handle the general mixture equation of state. The discretization also includes a suitable energy correction similar to that introduced in the previous section. We close the description of the discretization with a discussion of the evaluation of the mixture equation of state.

4.1 Overlapping grids and AMR

We assume that the flow domain is given by Ω and that it is discretized by an overlapping grid $\mathcal{G}$. The overlapping grid consists of a set of component grids $\{\mathcal{G}_i\}$, $i = 1, \ldots, \mathcal{N}_g$, that cover Ω and overlap where they meet. Each component grid covers a domain Ω_i in physical space and is defined by a mapping from physical space (x_1, x_2) in two dimensions to the unit square (r_1, r_2) in computational

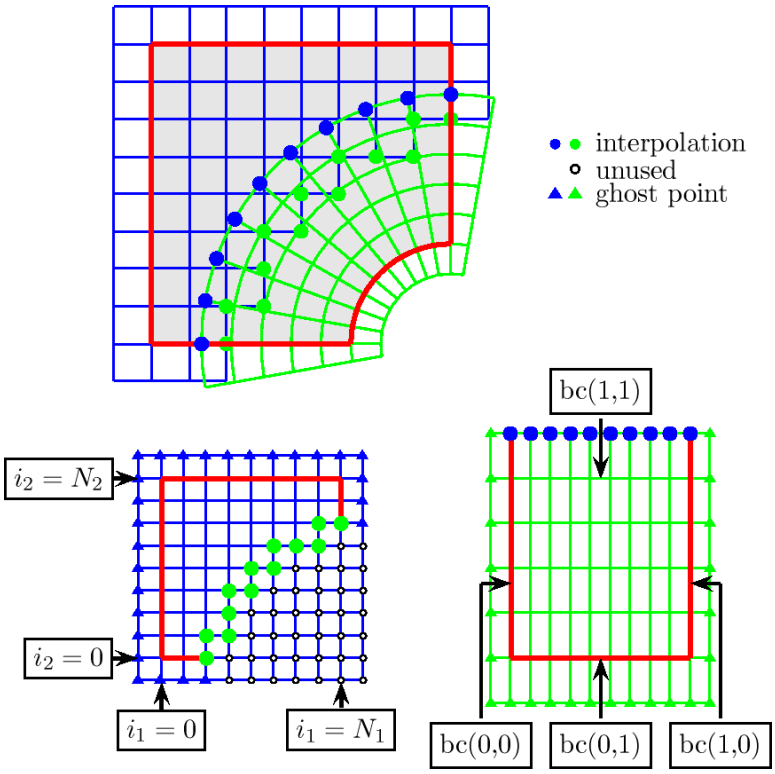

Fig. 3. The top view shows an overlapping grid consisting of two structured curvilinear component grids. The bottom views show the component grids in the unit square parameter space. Grid points are classified as discretization points, interpolation points (green or blue dots), or unused points (open disks). Ghost points (green or blue triangles) are used to apply boundary conditions. Here interpolation is performed in primitive quantities and the discretization includes a numerical source to the energy equation to maintain free-streaming flow.

space. Typically, the bulk of the flow domain is covered by one or more background Cartesian grids, while any curved boundaries of Ω are represented by narrow boundary-fitted curvilinear grids. This grid construction is quite general and numerically efficient because the majority of grid points belong to Cartesian grids (which are treated efficiently in our computational kernels).

A simple example of an overlapping grid is shown in Figure 3. In this example, the overlapping grid $\mathcal{G}$ consists of a background Cartesian grid and a boundary-fitted annular grid. The annular grid cuts a hole in the background grid rendering some grid points unused. These unused points are tagged and no computation is performed there. The remaining grid points are tagged as either interpolation points or discretization points. Interpolation points are those where the numerical solution is communicated between grids at the overlap. Discretization points are those where the discretization of the governing equations or boundary conditions are applied. The grid also employs ghost points to facilitate the numerical approximation of boundary conditions. The discretization used in this paper uses two layers of ghost points to support the width of the 5-point second-order Godunov stencil.

The interpolation at the grid overlap may be done using either primitive variables $\mathbf{w} = [\rho, u_1, u_2, p, \phi_a]^T$ or conservative variables $\mathbf{u} = [\rho, \rho u_1, \rho u_2, E, \rho\phi_a]^T$. The method described in [18] performs bi-linear interpolation in terms of conserved variables. For the numerical approximation of the multi-material

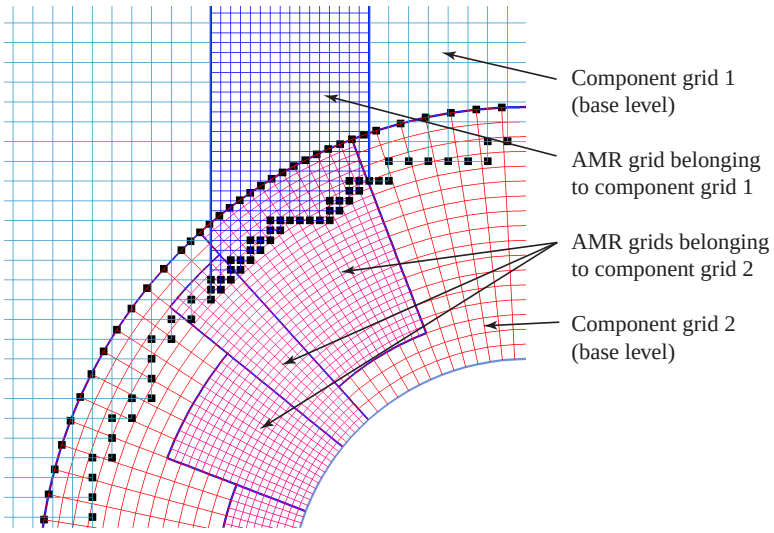

Fig. 4. Overlapping grids and AMR; a view of the overlap region showing the interpolation between refinement grids from different base grids. The black squares indicate interpolation points.

equations considered here, this choice does not maintain UPV flow since the pressure would not remain uniform in general, and thus interpolation of conservative variables would lead to numerical errors of the type described in the previous section. To avoid this error, we perform bi-linear interpolation of primitive variables.

Adaptive mesh refinement (AMR) is used in regions of the flow where the solution changes rapidly, such as near shocks and the interface between fluids. We employ a block-structured AMR approach following that described originally in [17] and using modifications for overlapping grids as presented in [18]. An estimate of the error is used to tag grid points for refinement. Following [18], we use

$$\mathbf{e_i} = \sum_{k=1}^{m} e_{\mathbf{i}}^{(k)}, \tag{24}$$

where m is the number of components ($m = 5$ in our case), and

$$e_{\mathbf{i}}^{(k)} = \frac{1}{2} \sum_{\alpha=1}^{2} \left(\frac{c_1}{s_k} \left| \Delta_{0\alpha} U_{\mathbf{i}}^{(k)} \right| + \frac{c_2}{s_k} \left| \Delta_{+\alpha} \Delta_{-\alpha} U_{\mathbf{i}}^{(k)} \right| \right) \tag{25}$$

is an estimate of the error in the k^{th} component of $U_{\mathbf{i}}$. In (25), s_k is a scale factor for $U_{\mathbf{i}}^{(k)}$, c_1 and c_2 are constants (weights), and $\Delta_{0\alpha}$, $\Delta_{+\alpha}$ and $\Delta_{-\alpha}$ are the un-divided central, forward and backward difference operators, respectively, in the α-direction in index space. The error estimate is computed for each component grid, and then smoothed and interpolated where the grids overlap. Refinement grid patches are created to cover all grids points where the smoothed error estimate is greater than a chosen tolerance. For example, Figure 4 shows the refinement grid structure near an overlap between grids. For the problems considered in this work, the material interface lies on the finest refinement level.

4.2 Discretization on a mapped grid

Each component grid, including base-level grids and any refined grids, is defined by a mapping from physical space (x_1, x_2) to the unit square in computational space (r_1, r_2). In computational space, equation (3) becomes

$$\frac{\partial}{\partial t}\mathbf{u} + \frac{1}{J}\frac{\partial}{\partial r_1}\mathbf{F}_1(\mathbf{u}) + \frac{1}{J}\frac{\partial}{\partial r_2}\mathbf{F}_2(\mathbf{u}) = 0, \tag{26}$$

where

$$\mathbf{F}_1(\mathbf{u}) = \frac{\partial x_2}{\partial r_2}\mathbf{f}_1 - \frac{\partial x_1}{\partial r_2}\mathbf{f}_2, \qquad \mathbf{F}_2(\mathbf{u}) = -\frac{\partial x_2}{\partial r_1}\mathbf{f}_1 + \frac{\partial x_1}{\partial r_1}\mathbf{f}_2,$$

and

$$J = \left|\frac{\partial(x_1, x_2)}{\partial(r_1, r_2)}\right|.$$

The metrics of the mapping, $\frac{\partial x_1}{\partial r_2}$, $\frac{\partial x_2}{\partial r_2}$, etc., and the Jacobian are known for each component grid. The discretization of (26) is performed using a uniform grid $(r_{1,i}, r_{2,j})$ with grid spacing $(\Delta r_1, \Delta r_2)$. The resulting quasi-conservative scheme is a generalization of (21) which for later purposes is written in the form

$$U_{i,j}^{n+1} = \hat{U}_{i,j}^{n+1} + \Delta G_{i,j}^{n+1}, \tag{27}$$

where

$$\hat{U}_{i,j}^{n+1} = U_{i,j}^{n} - \frac{\Delta t}{J\Delta r_1}\left(F_{1,i+1/2,j}^{n} - F_{1,i-1/2,j}^{n}\right) - \frac{\Delta t}{J\Delta r_2}\left(F_{2,i,j+1/2}^{n} - F_{2,i,j-1/2}^{n}\right). \tag{28}$$

Here, $U_{i,j}^{n}$ is an approximation to the cell average at $(r_{1,i}, r_{2,j})$ and at time $t = t_n$, $F_{1,i\pm1/2,j}^{n}$ and $F_{2,i,j\pm1/2}^{n}$ are numerical fluxes in the r_1 and r_2 directions, respectively, and $\Delta G_{i,j}^{n+1} = [0,\ 0,\ 0,\ \Delta E_{i,j}^{n+1},\ 0]^T$ involves an energy correction (as discussed in Section 4.2.2).

4.2.1 Numerical flux calculation

The fluxes in (28) may be computed in a number of ways. We choose a slope-limited Godunov method with an approximate Roe Riemann solver suitably modified to handle the general mixture equation of state which is defined implicitly but may be regarded in the form $e = e(\rho, p, \phi_a)$ or $p = p(\rho, \rho e, \rho\phi_a)$ whichever is convenient. (A description of the numerical evaluation of the equation of state is given in Section 4.2.3.) The basic approach for the flux calculation is similar to that used in [18] and so here we focus on the new elements of the calculation appropriate for the multi-material equations.

Let us consider, for example, the flux $F^n_{1,i+1/2,j}$ between grid cells $(r_{1,i}, r_{2,j})$ and $(r_{1,i+1}, r_{2,j})$. The first step involves the calculation of left and right states for the approximate Riemann solver. These are based on the Taylor expansions

$$\begin{aligned}
\mathbf{w}_L &= \mathbf{w}^n_{i,j} + \frac{\Delta r_1}{2}\left(\frac{\partial \mathbf{w}}{\partial r_1}\right)^n_{i,j} + \frac{\Delta t}{2}\left(\frac{\partial \mathbf{w}}{\partial t}\right)^n_{i,j} + \cdots, \\
\mathbf{w}_R &= \mathbf{w}^n_{i+1,j} - \frac{\Delta r_1}{2}\left(\frac{\partial \mathbf{w}}{\partial r_1}\right)^n_{i+1,j} + \frac{\Delta t}{2}\left(\frac{\partial \mathbf{w}}{\partial t}\right)^n_{i+1,j} + \cdots,
\end{aligned} \tag{29}$$

where $\mathbf{w} = [\rho, u_1, u_2, p, \phi_a]^T$ are the primitive variables corresponding to $\mathbf{u}$. These variables solve the quasi-linear equations

$$\frac{\partial \mathbf{w}}{\partial t} + A_1 \frac{\partial \mathbf{w}}{\partial r_1} + A_2 \frac{\partial \mathbf{w}}{\partial r_2} = 0, \tag{30}$$

where

$$A_1 = +\frac{1}{J}\frac{\partial x_2}{\partial r_2}\begin{bmatrix} u_1 & \rho & 0 & 0 & 0 \\ 0 & u_1 & 0 & 1/\rho & 0 \\ 0 & 0 & u_1 & 0 & 0 \\ 0 & c^2\rho & 0 & u_1 & 0 \\ 0 & 0 & 0 & 0 & u_1 \end{bmatrix} - \frac{1}{J}\frac{\partial x_1}{\partial r_2}\begin{bmatrix} u_2 & \rho & 0 & 0 & 0 \\ 0 & u_2 & 0 & 0 & 0 \\ 0 & 0 & u_2 & 1/\rho & 0 \\ 0 & 0 & c^2\rho & u_2 & 0 \\ 0 & 0 & 0 & 0 & u_2 \end{bmatrix},$$

$$A_2 = -\frac{1}{J}\frac{\partial x_2}{\partial r_1}\begin{bmatrix} u_1 & \rho & 0 & 0 & 0 \\ 0 & u_1 & 0 & 1/\rho & 0 \\ 0 & 0 & u_1 & 0 & 0 \\ 0 & c^2\rho & 0 & u_1 & 0 \\ 0 & 0 & 0 & 0 & u_1 \end{bmatrix} + \frac{1}{J}\frac{\partial x_1}{\partial r_1}\begin{bmatrix} u_2 & \rho & 0 & 0 & 0 \\ 0 & u_2 & 0 & 0 & 0 \\ 0 & 0 & u_2 & 1/\rho & 0 \\ 0 & 0 & c^2\rho & u_2 & 0 \\ 0 & 0 & 0 & 0 & u_2 \end{bmatrix}.$$

The square of the sound speed is given by

$$c^2 = \frac{\partial p}{\partial \rho} + \frac{\partial p}{\partial(\rho e)}\left(e + \frac{p}{\rho}\right) + \phi_a \frac{\partial p}{\partial(\rho\phi_a)}, \tag{31}$$

where the partial derivatives of p with respect to ρ, ρe and $\rho\phi_a$ are specified by the chosen equation of state for the mixture, see Section 4.2.3. In view of (30), the expansions in (29) become

$$\begin{aligned}
\mathbf{w}_L &= \mathbf{w}^n_{i,j} + \frac{\Delta r_1}{2}\left(I - \frac{\Delta t}{\Delta r_1}A^n_{1,i,j}\right)\left(\frac{\partial \mathbf{w}}{\partial r_1}\right)^n_{i,j} - \frac{\Delta t}{2}A^n_{2,i,j}\left(\frac{\partial \mathbf{w}}{\partial r_2}\right)^n_{i,j} + \cdots, \\
\mathbf{w}_R &= \mathbf{w}^n_{i+1,j} - \frac{\Delta r_1}{2}\left(I + \frac{\Delta t}{\Delta r_1}A^n_{1,i+1,j}\right)\left(\frac{\partial \mathbf{w}}{\partial r_1}\right)^n_{i+1,j} - \frac{\Delta t}{2}A^n_{2,i+1,j}\left(\frac{\partial \mathbf{w}}{\partial t}\right)^n_{i+1,j} + \cdots.
\end{aligned} \tag{32}$$

Sloped-limited approximations for the derivatives in (32) are defined in terms of characteristic variables. Let $A_k = R_k \Lambda_k R_k^{-1}$ be the eigenvalue decomposition of A_k, $k = 1$ or 2, and define

$$\begin{aligned}
\alpha_{i,j}^n &= \text{minmod}\left(\left(R_1^{-1}\right)_{i,j}^n (W_{i,j}^n - W_{i-1,j}^n)\,,\, \left(R_1^{-1}\right)_{i,j}^n (W_{i+1,j}^n - W_{i,j}^n) \right), \\
\beta_{i,j}^n &= \text{minmod}\left(\left(R_2^{-1}\right)_{i,j}^n (W_{i,j}^n - W_{i,j-1}^n)\,,\, \left(R_2^{-1}\right)_{i,j}^n (W_{i,j+1}^n - W_{i,j}^n) \right),
\end{aligned} \tag{33}$$

where $\text{minmod}(\cdot,\cdot)$ is the usual minimum-modulus function (applied componentwise) and $W_{i,j}^n$ are the primitive variables corresponding to $U_{i,j}^n$. These approximations are used in (32) to give

$$\begin{aligned}
W_L &= W_{i,j}^n + \frac{1}{2} R_{1,i,j}^n \left(I - \frac{\Delta t}{\Delta r_1} \max\{0, \Lambda_{1,i,j}^n\} \right) \alpha_{i,j}^n - \frac{\Delta t}{2\Delta r_2} R_{2,i,j}^n \Lambda_{2,i,j}^n \beta_{i,j}^n\,, \\
W_R &= W_{i+1,j}^n - \frac{1}{2} R_{1,i+1,j}^n \left(I + \frac{\Delta t}{\Delta r_1} \min\{0, \Lambda_{1,i+1,j}^n\} \right) \alpha_{i+1,j}^n - \frac{\Delta t}{2\Delta r_2} R_{2_i+1,j}^n \Lambda_{2,i+1,j}^n \beta_{i+1,j}^n\,,
\end{aligned} \tag{34}$$

which are the left and right states used to compute $F_{1,i+1/2,j}^n$. Similar calculations are used to obtain left and right states for the other numerical fluxes.

With left and right states in hand, we now consider an approximate one-dimensional Riemann problem in the r_1 direction given by

$$\frac{\partial \mathbf{u}}{\partial t} + B_1 \frac{\partial \mathbf{u}}{\partial r_1} = 0, \qquad |r_1| < \infty, \quad t > 0, \tag{35}$$

with

$$\mathbf{u}(r_1, 0) = \begin{cases} U_L & \text{if } r_1 \le 0, \\ U_R & \text{if } r_1 > 0, \end{cases}$$

where U_L and U_R the left and right states in conservative variables corresponding to W_L and W_R, respectively. Following the usual Roe prescription, the flux $F_{1,i+1/2,j}^n$ is taken from the exact solution of the approximate (linear) Riemann problem along $r_1 = 0$ for some suitably chosen matrix B_1 which depends on the left and right states. (In practice, we also employ a sonic fix as described in [24].) For the r_1 direction, we set

$$B_1 = \frac{\partial \mathbf{F}_1}{\partial \mathbf{u}}(\bar{\mathbf{u}}),$$

where $\bar{\mathbf{u}}$ is an averaged state chosen so that

$$\mathbf{F}_1(U_R) - \mathbf{F}_1(U_L) = B_1(U_R - U_L). \tag{36}$$

The matrix B_1 involves the velocity $(\bar{u}_1, \bar{u}_2)$, total enthalpy $\bar{h}$, mass fraction $\bar{\phi_a}$ of the averaged

state, and $(\bar{p}_\rho, \bar{p}_{\rho e}, \bar{p}_{\rho\phi_a})$ which approximate the partial derivatives p at the averaged state. Following [25], we set

$$\bar{z} = \frac{\sqrt{\rho}_L z_L + \sqrt{\rho}_R z_R}{\sqrt{\rho}_L + \sqrt{\rho}_R}, \qquad \text{for } z = (u_1, u_2, h, \phi_a).$$

For this choice, (36) reduces to the scalar constraint

$$\Delta p = \bar{p}_\rho \Delta\rho + \bar{p}_{\rho e}\Delta(\rho e) + \bar{p}_{\rho\phi_a}\Delta(\rho\phi_a), \tag{37}$$

where $\Delta p = p_R - p_L$, $\Delta\rho = \rho_R - \rho_L$, etc., are known. The remaining task is to define $\bar{p}_\rho$, $\bar{p}_{\rho e}$ and $\bar{p}_{\rho\phi_a}$ to satisfy (37), subject to mild conditions such as continuity as $U_R - U_L \to 0$.

The choice of the three derivatives satisfying (37) is not unique. Glaister offers one choice for the case of the single-component Euler equations, but an extension of this choice for the multi-material case could require the evaluation of the mixture equation of state for values of ϕ_a outside of the interval $[0, 1]$. An alternate approach which avoids this difficulty may be viewed geometrically as finding the point $(\bar{p}_\rho, \bar{p}_{\rho e}, \bar{p}_{\rho\phi_a})$ on the plane given by (37) which is closest to the mean values (p_1, p_2, p_3) defined by

$$p_1 = \frac{1}{2}\left\{\left(\frac{\partial p}{\partial\rho}\right)_L + \left(\frac{\partial p}{\partial\rho}\right)_R\right\}, \qquad p_2 = \frac{1}{2}\left\{\left(\frac{\partial p}{\partial(\rho e)}\right)_L + \left(\frac{\partial p}{\partial(\rho e)}\right)_R\right\},$$

and

$$p_3 = \frac{1}{2}\left\{\left(\frac{\partial p}{\partial(\rho\phi_a)}\right)_L + \left(\frac{\partial p}{\partial(\rho\phi_a)}\right)_R\right\}.$$

This construction gives

$$\bar{p}_\rho = p_1 + \theta\Delta\rho, \qquad \bar{p}_{\rho e} = p_2 + \theta\Delta(\rho e), \qquad \bar{p}_{\rho\phi_a} = p_3 + \theta\Delta(\rho\phi_a),$$

where

$$\theta = \frac{\Delta p - p_1\Delta\rho - p_2\Delta(\rho e) - p_3\Delta(\rho\phi_a)}{\sqrt{(\Delta\rho)^2 + (\Delta(\rho e))^2 + (\Delta(\rho\phi_a))^2}}.$$

In cases where $\sqrt{(\Delta\rho)^2 + (\Delta(\rho e))^2 + (\Delta(\rho\phi_a))^2} = 0$ we set $\theta = 0$ and thus $\bar{p}_\rho = p_1$, $p_{\rho e} = p_2$, and $\bar{p}_{\rho\phi_a} = p_3$.

The exact solution of (35) involves the eigenvalues and eigenvectors of B_1. Let

$$a_1 = \frac{1}{a_4}\frac{\partial x_2}{\partial r_2}, \qquad a_2 = -\frac{1}{a_4}\frac{\partial x_1}{\partial r_2}, \qquad a_3 = \frac{a_4}{J}, \tag{38}$$

where

$$a_4 = \sqrt{\left(\frac{\partial x_2}{\partial r_2}\right)^2 + \left(\frac{\partial x_1}{\partial r_2}\right)^2}.$$

The eigenvalues of B_1 are given by

$$\bar{\mu}_1 = a_3(\bar{w} - \bar{c}), \qquad \bar{\mu}_2 = \bar{\mu}_2 = \bar{\mu}_3 = a_3\bar{w}, \qquad \bar{\mu}_5 = a_3(\bar{w} + \bar{c}),$$

where $\bar{w} = a_1\bar{u}_1 + a_2\bar{u}_2$ is the component of the velocity of the averaged state normal to the curve $r_1 =$ constant and $\bar{c}$ is the sound speed given by

$$\bar{c}^2 = \bar{p}_\rho + \left(\bar{h} - \frac{1}{2}\left(\bar{u}_1^2 + \bar{u}_2^2\right)\right)\bar{p}_{\rho e} + \bar{\phi_a}\bar{p}_{\rho\phi_a}.$$

The right and left eigenvectors of B_1 belonging to the eigenvalues μ_1 and μ_5 are

$$\bar{\xi}_1 = \begin{bmatrix} 1 \\ \bar{u}_1 - a_1\bar{c} \\ \bar{u}_2 - a_2\bar{c} \\ \bar{h} - \bar{w}\bar{c} \\ \bar{\phi_a} \end{bmatrix}, \qquad \bar{\eta}_1 = \frac{1}{2\bar{c}^2}\begin{bmatrix} \bar{p}_\rho + \frac{1}{2}\left(\bar{u}_1^2 + \bar{u}_2^2\right)\bar{p}_{\rho e} + \bar{u}_n\bar{c} \\ -\bar{u}_1\bar{p}_{\rho e} - a_1\bar{c} \\ -\bar{u}_2\bar{p}_{\rho e} - a_2\bar{c} \\ \bar{p}_{\rho e} \\ \bar{p}_{\rho\phi_a} \end{bmatrix},$$

and

$$\bar{\xi}_5 = \begin{bmatrix} 1 \\ \bar{u}_1 + a_1\bar{c} \\ \bar{u}_2 + a_2\bar{c} \\ \bar{h} + \bar{w}\bar{c} \\ \bar{\phi_a} \end{bmatrix}, \qquad \bar{\eta}_5 = \frac{1}{2\bar{c}^2}\begin{bmatrix} \bar{p}_\rho + \frac{1}{2}\left(\bar{u}_1^2 + \bar{u}_2^2\right)\bar{p}_{\rho e} - \bar{u}_n\bar{c} \\ -\bar{u}_1\bar{p}_{\rho e} + a_1\bar{c} \\ -\bar{u}_2\bar{p}_{\rho e} + a_2\bar{c} \\ \bar{p}_{\rho e} \\ \bar{p}_{\rho\phi_a} \end{bmatrix},$$

respectively. The numerical flux is then given by

$$F^n_{1,i+1/2,j} = \begin{cases} F_1(U_L), & \text{if } \bar{\mu}_2 > 0 \text{ and } \bar{\mu}_1 \geq 0, \\ F_1(U_L) + \bar{q}_1\bar{\mu}_1\bar{\xi}_1, & \text{if } \bar{\mu}_2 > 0 \text{ and } \bar{\mu}_1 < 0, \\ F_1(U_R) - \bar{q}_5\bar{\mu}_5\bar{\xi}_5, & \text{if } \bar{\mu}_2 \leq 0 \text{ and } \bar{\mu}_5 > 0, \\ F_1(U_R), & \text{if } \bar{\mu}_2 \leq 0 \text{ and } \bar{\mu}_5 \leq 0, \end{cases} \tag{39}$$

where $\bar{q}_i = \bar{\eta}_i^T(U_R - U_L)$, $i = 1$ or 5.

4.2.2 Energy correction

The derivation of the energy correction in (27) follows closely the construction in Section 3 for one-dimensional flow. The basic idea is the same, but the details differ somewhat in order to cope with a general equation of state, the high resolution extension, and curvilinear grids. We consider the two step process in (27) and (28) with the temporary state $\hat{U}_{i,j}^{n+1}$ at time t_{n+1} being the result of a conservative shock-capturing scheme with fluxes calculated as outlined in Section 4.2.1. As such $\hat{U}_{i,j}^{n+1}$ is potentially contaminated by the type of error illustrated in Figure 1 and an energy correction is added to suppress this numerical error.

As before, we perform an auxiliary calculation for a suitable UPV flow to determine the size of the error. Let

$$\tilde{U}_{i,j}^{n+1} = U_{i,j}^{n} - \frac{\Delta t}{J\Delta r_1}\left(\tilde{F}_{1,i+1/2,j}^{n} - \tilde{F}_{1,i-1/2,j}^{n}\right) - \frac{\Delta t}{J\Delta r_2}\left(\tilde{F}_{2,i,j+1/2}^{n} - \tilde{F}_{2,i,j-1/2}^{n}\right). \tag{40}$$

where $\tilde{F}_{1,i\pm1/2,j}^{n}$ and $\tilde{F}_{2,i,j\pm1/2}^{n}$ are numerical fluxes obtained using left and right states corresponding to a UPV flow determined by the velocity and pressure of cell $(r_{1,i}, r_{2,j})$ at time t_n. For example, $\tilde{F}_{1,i+1/2,j}^{n}$ is computed with left and right states given by $\tilde{U}_L$ and $\tilde{U}_R$ corresponding to the slope-corrected primitive states W_L and W_R in (34) but with the velocity and pressure in both states replaced by $(u1_{i,j}^{n}, u2_{i,j}^{n})$ and $p_{i,j}^{n}$, respectively. The Riemann problem consists only of a contact discontinuity and thus the flux is given by

$$\tilde{F}_{1,i+1/2,j}^{n} = \begin{cases} F_1(\tilde{U}_L) & \text{if } a_3 w_{i,j}^{n} > 0 \\ F_1(\tilde{U}_R) & \text{if } a_3 w_{i,j}^{n} < 0 \end{cases}$$

where $w_{i,j}^{n} = a_1 u1_{i,j}^{n} + a_2 u2_{i,j}^{n}$ and (a_1, a_2, a_3) are given in (38). Similar formulas are used to obtain the remaining fluxes in (40).

We now have the necessary information to compute the energy correction in (27). The formula is an extension of the one in (22) for a general equation of state. Let $p_{i,j}^{n}$ and $\tilde{p}_{i,j}^{n+1}$ be the pressures computed from the states $U_{i,j}^{n}$ and $\tilde{U}_{i,j}^{n+1}$, respectively, and define

$$\Delta p_{i,j}^{n+1} = p_{i,j}^{n} - \tilde{p}_{i,j}^{n+1}.$$

The energy correction is then given by

$$\Delta E_{i,j}^{n+1} = \hat{\rho}_{i,j}^{n+1} e(\hat{\rho}_{i,j}^{n+1}, \hat{p}_{i,j}^{n+1} + \Delta p_{i,j}^{n+1}, \hat{\phi_a}_{i,j}^{\ n+1}) - \hat{\rho}_{i,j}^{n+1}\hat{e}_{i,j}^{n+1} \tag{41}$$

where $\hat{\rho}_{i,j}^{n+1}$, $\hat{p}_{i,j}^{n+1}$, $\hat{e}_{i,j}^{n+1}$ and $\hat{\phi_a}_{i,j}^{\ n+1}$ are the density, pressure, internal energy and mass fraction given by the state $\hat{U}_{i,j}^{n+1}$, respectively, and $e = e(\rho, p, \phi_a)$ is determined by the equation of state (as discussed in Section 4.2.3).

As noted earlier, the energy correction is nonzero only in regions of the flow where ϕ_a varies. Thus, for numerical efficiency the calculation of $\tilde{U}_{i,j}^{n+1}$ in (40) followed by $\Delta E_{i,j}^{n+1}$ in (41) is performed

only near the material interface. This region is narrow and represents a small fraction of the total number of grid points, and thus the added computational cost of the energy correction is small.

Finally, we note that the quasi-conservative scheme in (27) and (28) with the energy correction in (41) based on the slope-corrected states is second-order accurate for smooth flow. This will be demonstrated in Section 5.1 by comparing the numerical solution with exact smooth solutions constructed through the method of analytic solutions.

4.2.3 Evaluation of the equation of State

An evaluation of the equation of state for the mixture is required to obtain the pressure p and its first derivatives as a function of the conservative variables $(\rho, \rho e, \rho\phi_a)$ or the internal energy e as a function of the primitive variables (ρ, p, ϕ_a). This evaluation is needed to obtain the eigenvalues and eigenvectors for the slope corrections in (34), to compute the numerical flux in (39) based on the Roe-averaged state, and to determine the energy correction in (41). For the case of JWL equations of state for the pure constituents, the mixture rules in (7) give

$$\frac{1}{\rho} = \phi_a v_a + (1-\phi_a) v_b, \tag{42}$$

and

$$e = \phi_a \left[\frac{p v_a}{\omega_a} - \mathcal{F}_a(v_a) + \mathcal{F}_a(v_{0,a}) \right] + (1-\phi_a) \left[\frac{p v_b}{\omega_b} - \mathcal{F}_b(v_b) + \mathcal{F}_b(v_{0,b}) \right], \tag{43}$$

where v_k is the specific volume of material k, $k = a, b$, and $\mathcal{F}_k$ is defined in (5). In (43), we have assumed mechanical equilibrium so that $p_a = p_b = p$. The further assumption of thermal equilibrium gives

$$\frac{1}{C_{v,a}} \left[\frac{p v_a}{\omega_a} - \mathcal{Z}_a(v_a) + \mathcal{Z}_a(v_{0,a}) \right] = \frac{1}{C_{v,b}} \left[\frac{p v_b}{\omega_b} - \mathcal{Z}_b(v_b) + \mathcal{Z}_b(v_{0,b}) \right], \tag{44}$$

where $\mathcal{Z}_k$ is defined in (6). Equations (42), (43) and (44) provide three equations for the six unknowns ρ, p, e, ϕ_a, v_a and v_b, and these determine $p = p(\rho, \rho e, \rho\phi_a)$ or $e = e(\rho, p, \phi_a)$ implicitly upon elimination of v_a and v_b.

For the special case of ideal gases in which $\mathcal{F}_k = \mathcal{Z}_k = 0$, $k = a, b$, the equation of state for the mixture is given explicitly in (9). Further, the partial derivatives of p with respect to the conservative variables are given by

$$\frac{\partial p}{\partial \rho} = \frac{e\phi_a C_{v,a} C_{v,b} (\gamma_b - \gamma_a)}{\left(\phi_a C_{v,a} + (1-\phi_a) C_{v,b}\right)^2}, \qquad \frac{\partial p}{\partial (\rho e)} = \gamma(\phi_a) - 1,$$

and

$$\frac{\partial p}{\partial (\rho\phi_a)} = -\frac{e C_{v,a} C_{v,b} (\gamma_b - \gamma_a)}{\left(\phi_a C_{v,a} + (1-\phi_a) C_{v,b}\right)^2},$$

where $\gamma(\phi_a)$ is given in (10).

For the more general case in which $\mathcal{F}_k$ and $\mathcal{Z}_k$ are not zero, a numerical evaluation is necessary. This may be done using an application of Newton's method which gives $p = p(\rho, \rho e, \rho\phi_a)$ or $e = e(\rho, p, \phi_a)$ approximately. (In practice, we also save converged values for the extra variables v_a and v_b at all grid points so that they may be used as initial guesses for Newton iterations at the next time step.) Once converged values are found, the partial derivatives of p with respect to ρ, ρe and $\rho\phi_a$ may be obtained from the linear system of equations implied by an implicit differentiation of (42), (43) and (44).

5 Numerical Results

We now present numerical results using the numerical method described in Section 4. The discussion begins with a study of the behavior and accuracy of the numerical approach for cases in which exact solutions are known. We then proceed in the latter subsections to more complicated problems where exact solutions are not known.

5.1 Smooth two-dimensional flow

We first present a convergence study of the numerical method for the case when the solution is smooth. Such a solution is difficult to obtain in general, but may be constructed using the method of analytic solutions for a modified set of equations. The idea is to pick a smooth function and then add a forcing term to the right-hand-side of (3) so that the function becomes an exact solution of the modified equations. We then make a straightforward extension to the numerical method to handle the forcing term. This approach is quite general and is very useful to check the implementation of any numerical method and to verify its convergence rate.

Let $\mathbf{u}_s(x_1, x_2, t)$ be a chosen smooth function, and consider the modified equations

$$\frac{\partial}{\partial t}\mathbf{u} + \frac{\partial}{\partial x_1}\mathbf{f}_1(\mathbf{u}) + \frac{\partial}{\partial x_2}\mathbf{f}_2(\mathbf{u}) = \mathbf{h}(\mathbf{u}_s), \tag{45}$$

where $\mathbf{u}$, $\mathbf{f}_1$ and $\mathbf{f}_2$ are defined as in (3), and

$$\mathbf{h}(\mathbf{u}_s) = \frac{\partial}{\partial t}\mathbf{u}_s + \frac{\partial}{\partial x_1}\mathbf{f}_1(\mathbf{u}_s) + \frac{\partial}{\partial x_2}\mathbf{f}_2(\mathbf{u}_s).$$

An equation of state is needed to complete the system of equations and we assume the one for a mixture of two ideal gases given in (9). Clearly, $\mathbf{u} = \mathbf{u}_s$ is a solution of (45), and many choices for

$\mathbf{u}_s$ can be made for the purpose of a convergence study. For example, let

$$\left.\begin{aligned}
\rho_s &= \frac{1}{8}\cos\left(\pi\left(x_1-\tfrac{1}{2}\right)\right)\cos(\pi x_2)\cos(\pi t)+1 \\
u_{1,s} &= \cos(\pi x_1)\cos(\pi x_2)\cos(\pi t) \\
u_{2,s} &= \frac{1}{2}\cos\left(\pi\left(x_1-\tfrac{1}{2}\right)\right)\cos\left(\pi\left(x_2-\tfrac{1}{2}\right)\right)\cos(\pi t) \\
p_s &= \rho_s\left[\frac{1}{4}\cos(\pi x_1)\cos\left(\pi\left(x_2-\tfrac{1}{2}\right)\right)\cos(\pi t)+1\right] \\
\phi_{a,s} &= \frac{1}{8}\cos(\pi x_1)\cos(\pi x_2)\cos(\pi t)+\frac{1}{2}
\end{aligned}\right\} \tag{46}$$

be the density, velocity, pressure and mass fraction used to construct the conservative variables in $\mathbf{u}_s$. Here, we use $\gamma_a = 3.0$, $\gamma_b = 1.4$, $C_{v,a} = 2.4$ and $C_{v,b} = 4.2$ for the ratio of specific heats for the mixture given in (10).

We consider the numerical solution of (45) for two different domains. The first domain is a square with $|x_k| \le 2$, $k = 1, 2$. For this domain (and for later examples) we use a Cartesian grid defined by

$$\begin{aligned}
\mathcal{R} = \{&(x_{1,c} + i_1\Delta x_1\,,\, x_{2,c} + i_2\Delta x_2)\,| \\
&\Delta x_k = (x_{k,d} - x_{k,c})/N_k,\, i_k = 0, 1, \ldots, N_k,\, k = 1, 2\}.
\end{aligned} \tag{47}$$

Here, we use $x_{1,d} = x_{2,d} = -x_{1,c} = -x_{2,c} = 2$ and $N_1 = N_2 = 40m$, where m is an integer indicating grid size. The initial condition is taken to be $\mathbf{u}_s(x_1, x_2, 0)$ and the boundary conditions on the perimeter of the square are given by the exact solution. We integrate the modified equations numerically for $0 \le t \le 1$ and compute the error. For this calculation, we replace the minmod limiter in (33) with an average of the two arguments of the function. This is done so that the convergence test is not adversely affected by a loss of accuracy near local extrema in the smooth solution. Table 1 shows the maximum error in the primitive variables at $t = 1$ for various grid resolutions determined by m. Assuming that the error for a variable w, say, behaves according to $e_w(m) = Kh_m^\alpha$, where K is a constant and h_m is a representative grid spacing for a given m, the convergence rate α can be estimated by a least squares fit to the computed errors. These convergence rates are shown in the table and we note that second-order convergence is achieved for each of the variables.

The second domain is a circular disk of radius 0.8 which is covered by an overlapping grid consisting of a Cartesian grid given by (47) and an annular grid defined by

$$\begin{aligned}
\mathcal{A} = \{&(r_c + i_r\Delta r\,,\, \theta_c + i_\theta\Delta\theta)\,|\,\Delta r = (r_d - r_c)/N_r, \\
&\Delta\theta = (\theta_d - \theta_c)/N_\theta,\, i_k = 0, 1, \ldots, N_k,\, k = r, \theta\}.
\end{aligned} \tag{48}$$

For this overlapping grid, we use $r_c = 0.4$, $r_d = 0.8$, $\theta_c = 0$, $\theta_d = 2\pi$, $N_r = 10m$ and $N_\theta = 80m$ for the boundary-fitted annular grid, and $x_{1,d} = x_{2,d} = -x_{1,c} = -x_{2,c} = 0.6$ and $N_1 = N_2 = 30m$

m	$e_\rho(m)$	$e_{u_1}(m)$	$e_{u_2}(m)$	$e_p(m)$	$e_{\phi_a}(m)$
1	1.3e−2	1.9e−2	8.1e−3	1.0e−2	9.5e−4
2	3.0e−3	5.2e−3	2.2e−3	2.8e−3	2.6e−4
4	7.7e−4	1.4e−3	6.0e−4	7.8e−4	7.0e−5
8	2.0e−4	3.7e−4	1.8e−4	2.1e−4	2.0e−5
α	2.0	1.9	1.8	1.9	1.9

Table 1
Convergence results for the square domain. Maximum errors in density, velocity components, pressure and mass fraction at $t = 1$ for grid resolutions determined by m, and the estimated convergence rate α for each variable.

for the background Cartesian grid. This test provides a further check of the implementation of the scheme for a curvilinear grid and checks the accuracy of the interpolation at the grid overlap. Table 2 shows the maximum error in the primitive variables at $t = 1$ for various resolutions of the overlapping grid. As before we note that second-order convergence is achieved for each of the variables.

m	$e_\rho(m)$	$e_{u_1}(m)$	$e_{u_2}(m)$	$e_p(m)$	$e_{\phi_a}(m)$
1	2.2e−3	4.6e−3	2.5e−3	1.6e−3	9.7e−4
2	5.3e−4	1.1e−3	5.6e−4	4.2e−4	2.3e−4
4	1.3e−4	2.7e−4	1.2e−4	1.2e−4	5.8e−5
8	3.1e−5	6.5e−5	3.3e−5	3.3e−5	1.4e−5
α	2.1	2.0	2.1	1.9	2.0

Table 2
Convergence results for the circular domain. Maximum errors in density, velocity components, pressure and mass fraction at $t = 1$ for grid resolutions determined by m, and the estimated convergence rate α for each variable.

5.2 1-D Shock-Interface Interactions

Having shown the convergence of the numerical method for smooth solutions, we now turn our attention to problems involving a sharp interface between pure materials and the interaction of the interface with shocks. For such problems, the numerical scheme is conservative in the regions on either side of the material interface where $\phi_a = 0$ or $\phi_a = 1$ (and away from grid overlaps). Near the interface, the energy correction is applied to suppress numerical oscillations and there the numerical scheme is quasi-conservative as pointed out in Section 3. Discrete conservation is particularly important in the vicinity of shocks and so it is of interest to study the behavior of the numerical method for problems in which the interface and shocks interact. As in the previous study, we focus on problems for which exact solutions are available. This is done first for a one-dimensional problem involving ideal gases. A two-dimensional case involving JWL equations of state is considered in the next section.

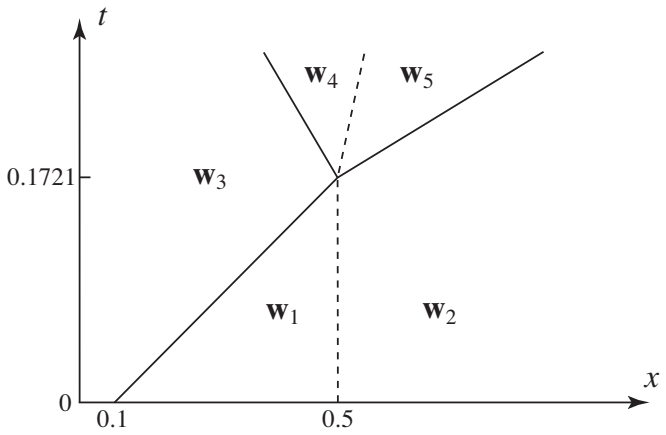

Fig. 5. An x-t diagram for the one-dimensional shock-interface interaction problem. An incident shock (solid line) collides with an interface (dashed line) resulting in a transmitted and reflected shocks

For the one-dimensional problem, we consider an interface initially located at $x = 0.5$ separating materials with $\gamma_a = 1.35$ and $C_{v,a} = 2.4$ to the left and $\gamma_b = 5.0$ and $C_{v,b} = 1.5$ to the right. These values correspond roughly to high explosive products (material a) and a confining material (material b), see [26]. To the left of the interface in material a there is a shock, initially at $x = 0.1$, traveling to the right with speed 2.324 relative to the interface. At time $t = 0.1721$, the interface and shock collide resulting in a transmitted shock traveling to the right in material b and a reflected shock traveling to the left in material a. An x-t diagram for the problem in the reference frame of the interface is shown in Figure 5 and the primitive states separated by the shocks and the material interface are indicated. For the chosen states $\mathbf{w}_1$ and $\mathbf{w}_2$ on either side of the interface at $t = 0$ and for a chosen shock Mach number equal to 2, the remaining states can be obtained by solving suitable Riemann problems. All of these states are collected in Table 3.

	Region 1	Region 2	Region 3	Region 4	Region 5
ρ	1	1.9	2.7647	3.9581	2.5786
u	0	0	1.4833	0.9304	0.9304
p	1	1	4.4468	7.2498	7.2498
ϕ_a	0	1	0	0	1

Table 3
Primitive states for the regions of the flow shown in Figure 5 for the one-dimensional shock-interface interaction problem.

We consider two numerical experiments involving the configuration shown in Figure 5. In both experiments, the usual small start-up errors in the other characteristic fields associated with taking a perfect jump for the initial shock are filtered out so as not to corrupt later interactions with the material interface. For the first experiment, the interface is moving to the right with a speed equal to 0.1 relative to the fixed lab frame of the grid. Since an isolated interface will slowly widen, the interface is smeared over a few grid cells in the numerical solution. Prior to the collision with the shock, the local behavior of the numerical solution near the interface is similar to that shown in Figure 1 for the uncorrected scheme and to that shown in Figure 2 for the corrected scheme. The numerical errors in the solution for the uncorrected scheme persist after the shock and interface

collide, and new errors arise due to the interaction. Figure 6 shows the behavior of the solution of the uncorrected scheme at a time $t = 0.25$ after collision for a fine grid with 1600 grid cells on the interval $[0, 1]$. Here we note, in particular, a large undershoot in the density just to the right of the interface which is a result of the interaction, and a relatively small blip in all of the variables to the left of the reflected shock which is a remnant of the error generated near the interface prior to the interaction.

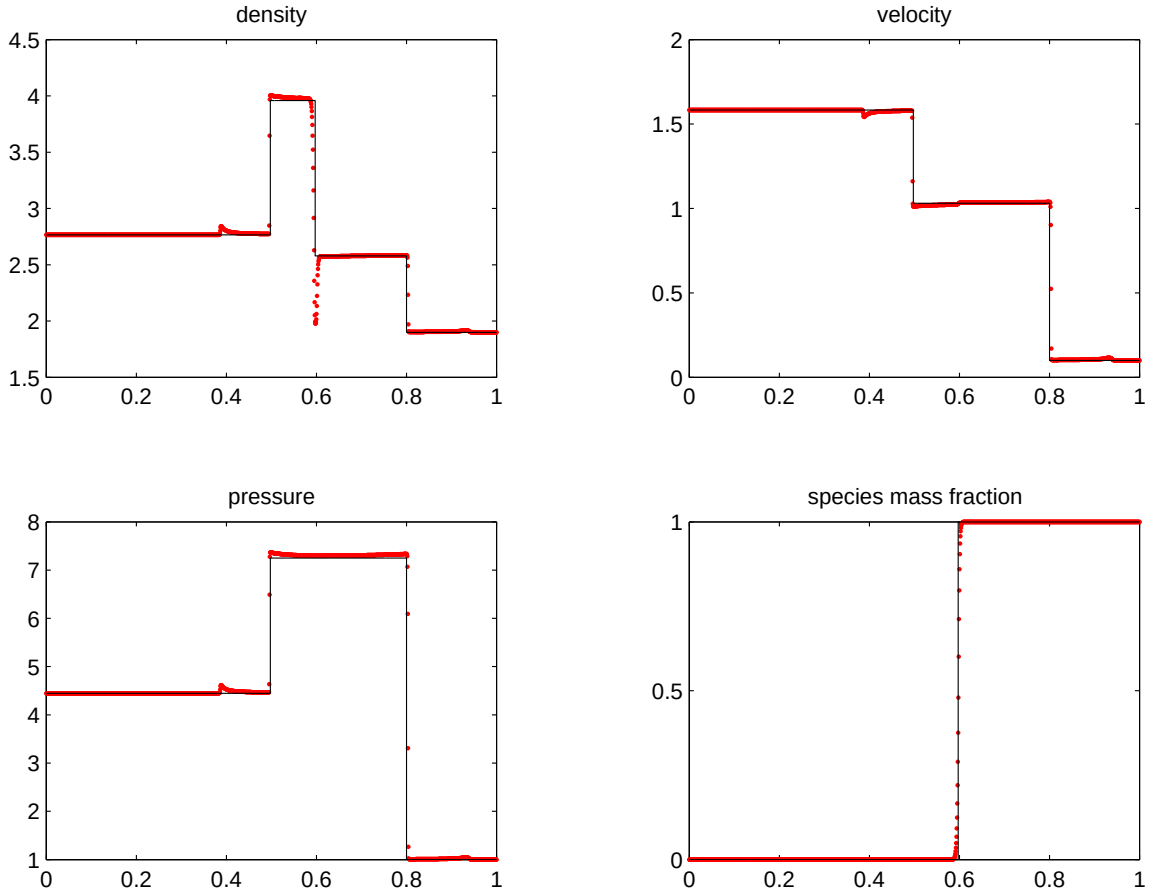

Fig. 6. Numerical solution of the uncorrected scheme at $t = 0.25$ for a one-dimensional interface-shock interaction problem with a uniform velocity equal to 0.1 ahead of the incident shock. The exact solution is shown in black and the numerical solution is shown by the red marks.

Figure 7 shows the numerical solution for the same problem but with the energy correction term included. Here we note that after the collision the behavior of the numerical solution near the interface remains in good agreement with the exact solution. The behavior and position of the transmitted and reflected shocks are in good agreement with the exact solution as well. Since the shock and interface interact for only a few grid cells in space and time, there is only a short period over which the non-conservative correction could influence the position of the shock. It is observed that the overall contribution from the energy correction has no significant affect on shock position, supporting the argument made previously. A closer look at the behavior near the interface and shocks in Figure 8 for various grid resolutions shows the convergence of the method toward the exact solution.

A further test of the method can be done by considering a second numerical experiment in which

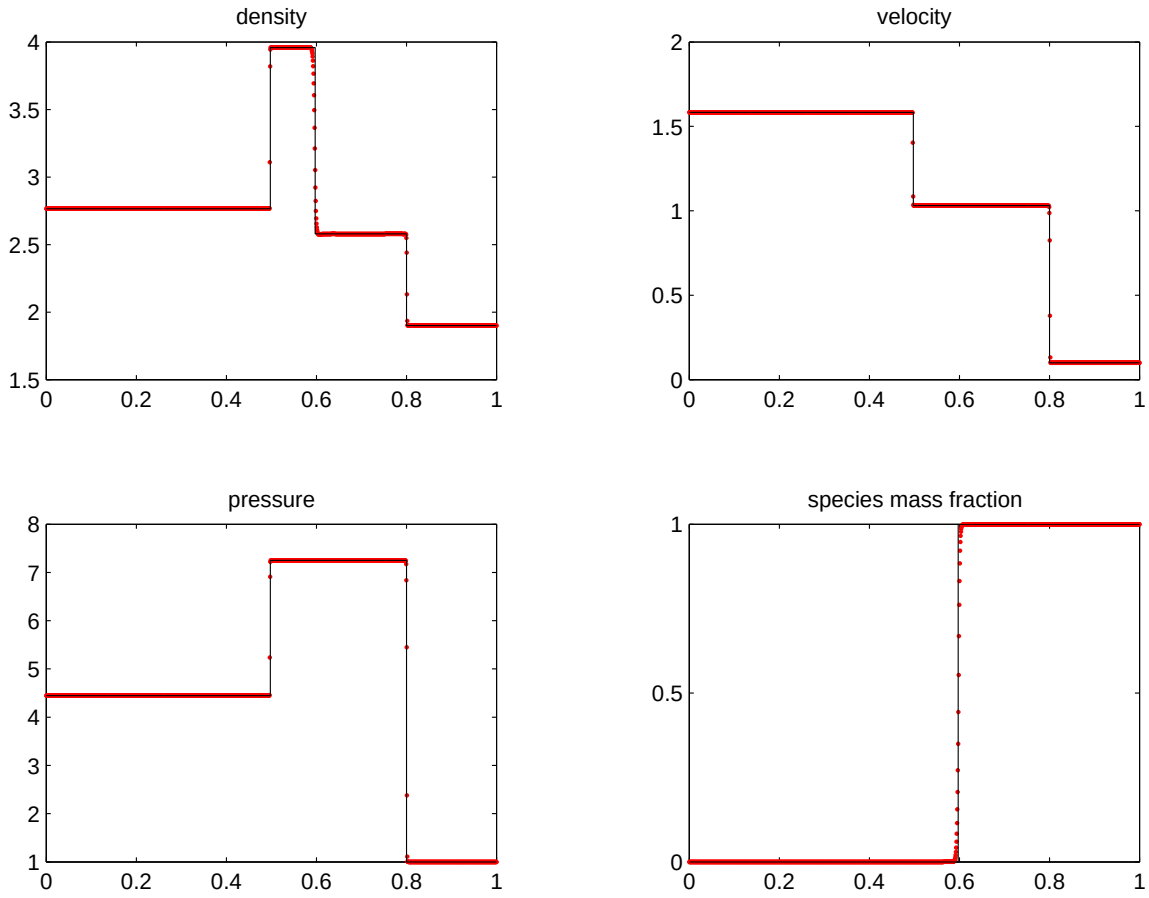

Fig. 7. Numerical solution of the energy-corrected scheme at $t = 0.25$ for a one-dimensional interface-shock interaction problem with a uniform velocity equal to 0.1 ahead of the incident shock. The exact solution is shown in black and the numerical solution is shown by the red marks. The grid resolution is the same as that shown in Figure 6

the interface is at rest with respect to the grid prior to shock collision. In this case, the interface remains sharp for both the uncorrected and corrected schemes prior to collision. Hence, any error that appears in the numerical solution after the collision is entirely a result of the interaction. Figure 9 shows a comparison of the density for the uncorrected and corrected schemes at $t = 0.25$. Here, we see that the solution of the energy-corrected scheme remains in excellent agreement with the exact solution. (Excellent agreement is also found in the other primitive variables.) The solution of the uncorrected scheme, on the other hand, shows a large undershoot similar to that observed in Figure 6. We also note that the solution from the uncorrected scheme contains a small error in the position of the transmitted shock and an overshoot in the state behind the reflected shock.

For the previous experiments, we considered the numerical solution for a single component grid. It is also of interest to consider the effect of a grid overlap on the behavior of the numerical solution of the energy-corrected scheme. In order to examine this behavior, we consider an overlapping grid consisting of two component grids that overlap at $x = 0.5$. The grids are constructed so that the grid spacing is the same Δx for each grid, but there is a mismatch of $\Delta x/2$ at the overlap so that the interpolation at the overlap plays a role in the calculation. For the case when the flow is at rest relative to the grid ahead of the shock, the interface sits on the overlap until $t = 0.1721$ when the

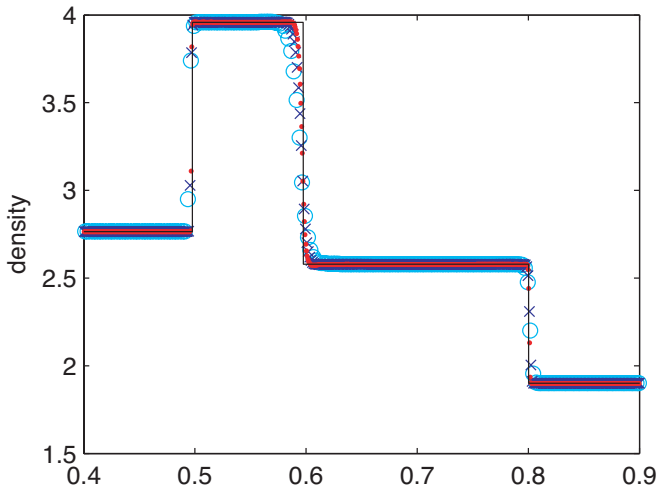

Fig. 8. Grid convergence of density at $t = 0.25$ for the energy-corrected scheme for a one-dimensional interface-shock interaction problem with a uniform velocity equal to 0.1 ahead of the incident shock. Numerical solutions with 400 (circles), 800 (crosses) and 1600 (dots) grid cells are shown.

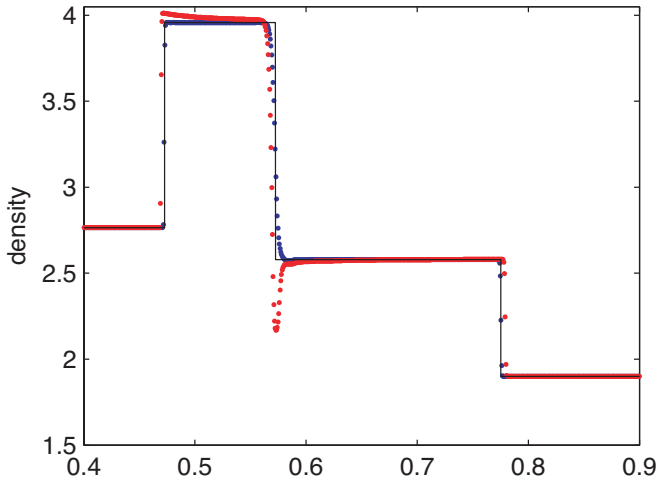

Fig. 9. Comparison of density at $t = 0.25$ for a one-dimensional interface-shock interaction problem with no background velocity ahead of the incident shock. The black curve shows the exact solution and the red and blue marks show numerical solutions of the uncorrected and corrected schemes, respectively.

shock collides with it. Prior to the collision there is no significant error in the numerical solution near the interface. After the collision the behavior of the solution is similar to that obtained for the calculation without the overlap. For example, Figure 10 shows the behavior of the density at $t = 0.25$ for the numerical solution of the energy-corrected scheme with and without a grid overlap. Both of these solutions are in excellent agreement with the exact solution.

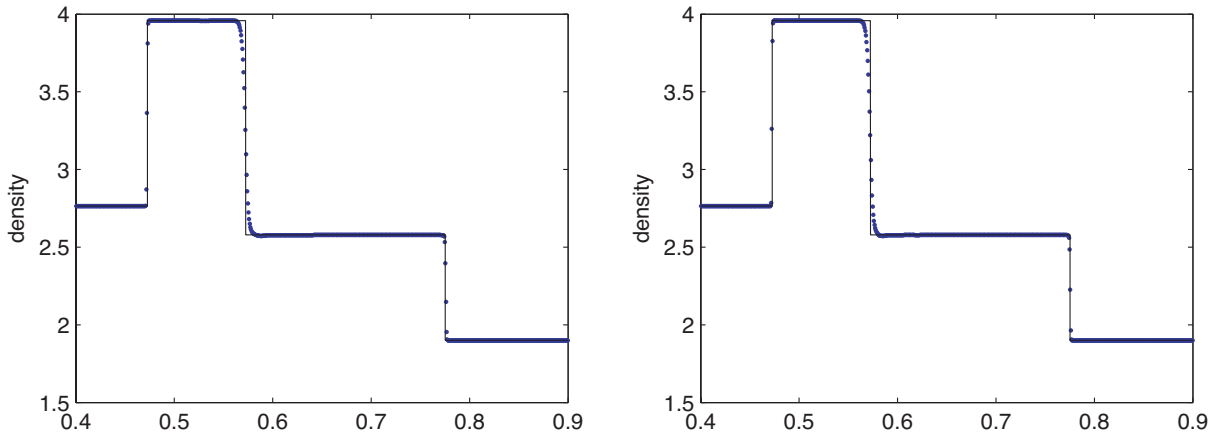

Fig. 10. Density at $t = 0.25$ for a one-dimensional interface-shock interaction problem with no background velocity ahead of the incident shock. Numerical solution for an overlapping grid (left) and one component grid (right). The black curve shows the exact solution and the blue marks show numerical solution for both cases.

5.3 2-D Shock-Interface Interactions

We now investigate the behavior of the present scheme for a two-dimensional flow involving the interaction of an oblique shock with a material interface. The configuration of the problem is shown in Figure 11. A planar interface separates material a above given by the primitive state $\mathbf{w}_1$ (with $\phi_{a,1} = 1$) and material b below given by the primitive state $\mathbf{w}_2$ (with $\phi_{a,2} = 0$). The states are in pressure equilibrium, i.e. $p_1 = p_2$, and the normal component of the velocity is zero for both states. An oblique shock deflects the flow by angle θ. The states downstream of the shock, $\mathbf{w}_3$ and $\mathbf{w}_4$, are also in pressure equilibrium, i.e. $p_3 = p_4$, with zero normal flow relative to the deflected interface. The angles of the oblique shocks relative to the vertical in materials a and b are given by ξ and η, respectively. We are motivated to consider this configuration for two reasons. First, the exact solution may be constructed using a shock-polar analysis of the flow on either side of the interface, and thus this becomes a suitable test case for the numerical scheme for a non-trivial two-dimensional flow. Second, the configuration is related to the local behavior of a detonation near a strong inert confinement (see [27]).

The solution for the flow can be constructed by considering the oblique shock jump conditions for the pure materials on either side of the interface. In material a, for example, the shock conditions give

$$\left.\begin{aligned} q_1 \sin\xi &= q_3 \sin(\xi+\theta_3) \\ \rho_1 q_1 \cos\xi &= \rho_3 q_3 \cos(\xi+\theta_3) \\ p_1 + \rho_1 (q_1\cos\xi)^2 &= p_3 + \rho_3 (q_3\cos(\xi+\theta_3))^2 \\ h_1 + \tfrac{1}{2}(q_1\cos\xi)^2 &= h_3 + \tfrac{1}{2}(q_3\cos(\xi+\theta_3))^2 \end{aligned}\right\} \tag{49}$$

where ρ_i, q_i, p_i and $h_i = e_i + p_i/\rho_i$, $i = 1, 3$ are the density, magnitude of the velocity, pressure

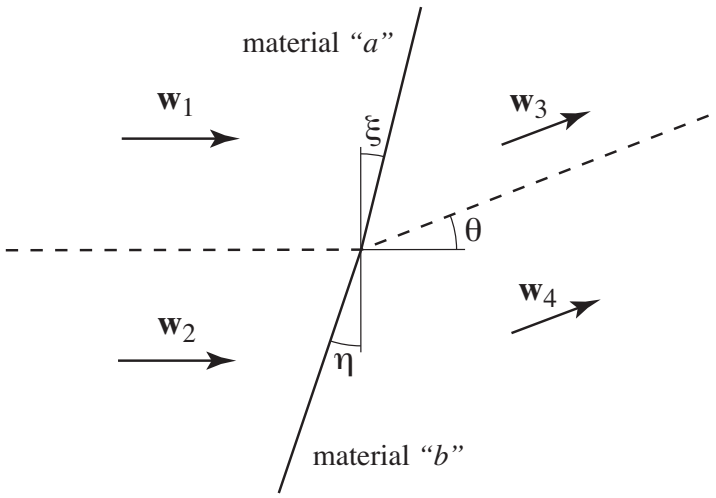

Fig. 11. Oblique shock interaction with a planar material interface. The interface (dashed line) separates material a above from material b below, and is deflected by an angle θ behind the shock. The oblique shock (solid line) make angles ξ and η relative to the vertical.

and enthalpy, respectively, and θ_3 is the flow deflection in region 3. The equation of state gives $e_i = e_a(\rho_i, p_i)$, $i = 1, 3$, where e_a is the internal energy for material a. For a given upstream state, these equations determine the downstream state as a function of the shock angle ξ. A similar set of equations determines the downstream state in material b as a function of the shock angle η for a given upstream state. These two shock angles are then determined by the condition that $p_3 = p_4$ and $\theta_3 = \theta_4 = \theta$.

For example, let us consider two materials described by the JWL equations of state given in (4) with stiffening functions, $\mathcal{F}_k$ and $\mathcal{Z}_k$, $k = a$ or b, given in (5) and (6), respectively. The parameters in these functions are taken to be $\omega_a = 0.8938$, $A_a = 692.5067$, $B_a = -.044776$, $R_{1,a} = 11.3$, $R_{2,a} = 1.13$, $C_{v,a} = 1.0$ and $v_{0,a} = 0.5$ for material a, and $\omega_b = 0.5$, $A_b = 13.1813$, $B_b = 0.5677291$, $R_{1,b} = 6.2$, $R_{2,b} = 2.2$, $C_{v,b} = .40209$ and $v_{0,b} = 0.5$ for material b. This choice corresponds approximately to the explosive LX-17 reactants (material a) and products (material b) [20]. For a given upstream state the pressure and flow deflection in the downstream state on either side of the interface may be computed versus the shock angle. These shock polars are shown in Figure 12 for the upstream state given in Table 4. The solution is determined by the intersection of the these curves where $p_3 = p_4$ and $\theta_3 = \theta_4 = \theta$. At this intersection, $\xi = 0.2141538$, $\eta = 0.2485619$ and $\theta = 0.1$, and the corresponding state of the flow is also given in Table 4. In this solution, we choose the upstream states so that $q_3 = q_4$ which implies that the normal and tangential components of the velocity are equal across the interface in the flow behind the shock. This choice is made for numerical convenience as it avoids the Kelvin-Helmholtz instability that would develop for the case when the tangential component of the velocity is not equal across the interface. Upstream of the shock there is a slip across the interface, but this occurs along a grid line. The numerical approximation for this situation is exact and so there is negligible growth of the instability here. The solution also includes a uniform translation equal to 0.5 in the negative x_1-direction as an added test of the numerical scheme.

Numerical solutions are computed for $0 \le t \le 1$ using the exact solution given in Table 4 centered about the origin as initial conditions. The computation is performed on a rectangular grid $\mathcal{R}$ defined by (47) with $x_{1,d} = x_{2,d} = -x_{1,c} = -x_{2,c} = 2$ and $N_1 = N_2 = 160$. Three AMR grid resolutions

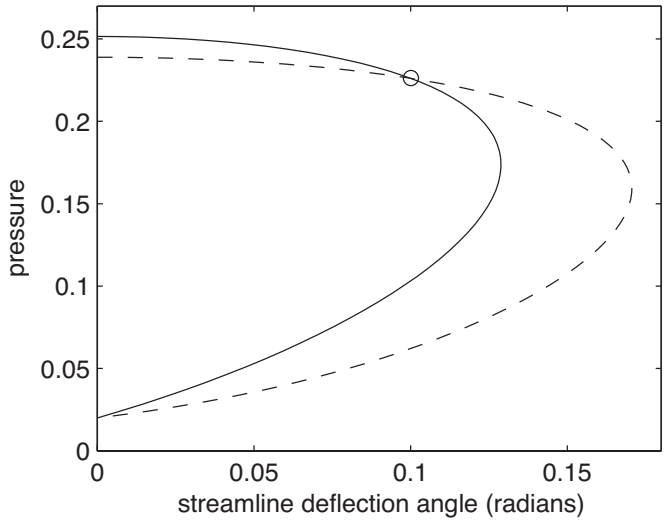

Fig. 12. Shock polars for the flow configuration shown in Figure 11. The dashed curve shows the downstream pressure p_3 versus flow deflection θ_3 parameterized by the shock angle ξ for material a while the solid curve is p_4 versus θ_4 parameterized by η for material b. The exact solution with states given in Table 4 is given by the point of intersection of the these shock polars where $p_3 = p_4 = 0.226085$, $\theta_3 = \theta_4 = 0.1$, $\xi = 0.2141538$ and $\eta = 0.2485619$.

	Region 1	Region 2	Region 3	Region 4
ρ	0.9	1.1	1.344539	1.574952
u_1	0.3516656	0.3131895	0.0828007	0.0828007
u_2	0	0	0.0584751	0.0584751
p	0.02	0.02	0.226085	0.226085
ϕ_a	1	0	1	0

Table 4
Primitive variables for the flow configuration shown in Figure 11. The velocities include a constant translation to the left with speed 0.5

are investigated. The first uses only the base grid $\mathcal{R}$, the second uses $\mathcal{R}$ and one AMR level with refinement factor 4, and the third uses 2 AMR levels each with refinement factor 4. This results in effective grid resolutions given by $N_1 = N_2 = 160$, 640, and 2560, respectively. At time $t = 1$ the structure is centered at $x_1 = -0.5$, $x_2 = 0$, and our main focus is on the behavior of the numerical solution in this vicinity. Thus, for the purposes of this test, the boundaries of the domain are chosen far enough away so that the choice of the boundary conditions has no effect on this local solution at $t = 1$.

Figure 13 shows color contours of density and pressure of the numerical solution at $t = 0$ and $t = 1$. The solutions shown are at the finest resolution and the corresponding AMR grid structures at $t = 0$ and $t = 1$ are also shown in the figure. The local structure near the intersection of the interface and the oblique shock appears to translate unchanged in the numerical solution in agreement with the exact solution. In particular, we observe no numerical oscillations in the pressure near the material interface at $t = 1$. We note that there are regions near the bottom and top of the computational

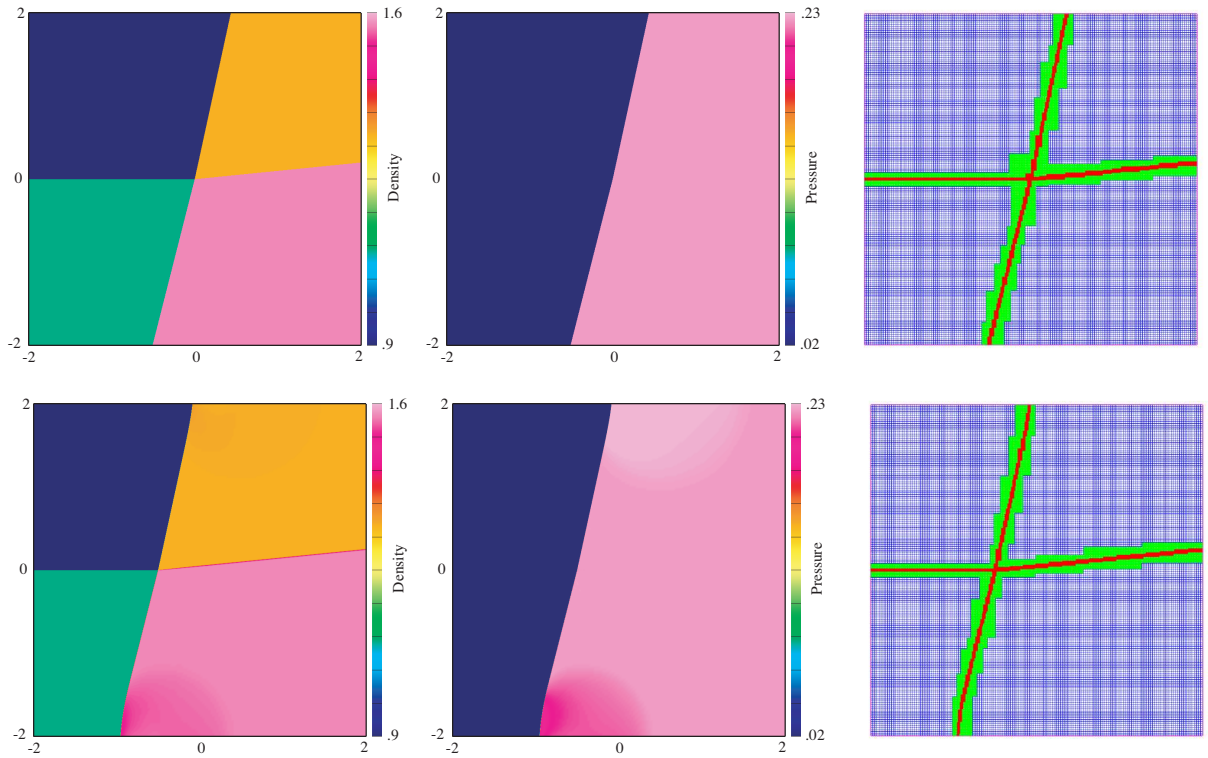

Fig. 13. Numerical solution at $t = 0$ (top row) and $t = 1$ (bottom row) for the interaction of an oblique shock interaction with a planar material interface. The left column shows the density, the middle column shows the pressure, and the right column is the AMR grid for each calculation.

domain at $x_2 = -2$ and $x_2 = 2$, respectively, and behind the shock where the flow is not uniform. These regions, seen as slight shadows in the shaded contour plots in the figure, are due to the interaction of the shock and the boundary, but do not effect the solution near the interaction of the shock and interface.

A closer look at the numerical solution at $t = 1$ is made by taking one-dimensional slices along the lines $x_1 = -0.25$, $x_2 = 0.5$, and $x_2 = -0.5$. Figure 14 shows the density along $x_1 = -0.25$ for the numerical solution at the finest resolution. This slice focuses on the behavior near the material interface downstream of the shock, and we note excellent agreement with the exact solution. For comparison purposes, we also show the behavior of the numerical solution given by the uncorrected scheme with the same grid resolution. This uncorrected solution shows a large undershoot near the interface similar to that observed previously in the one-dimensional shock interaction problem.

Figure 15 shows grid convergence of the pressure along the lines $x_2 = 0.5$ and $x_2 = -0.5$. These lines are close enough to the intersection of the shock and the interface so that the solution would be effected by any errors generated along $x_2 = 0$. It is seen that shock locations are in good agreement with the exact solution and that no errors appear from the interface along $x_2 = 0$.

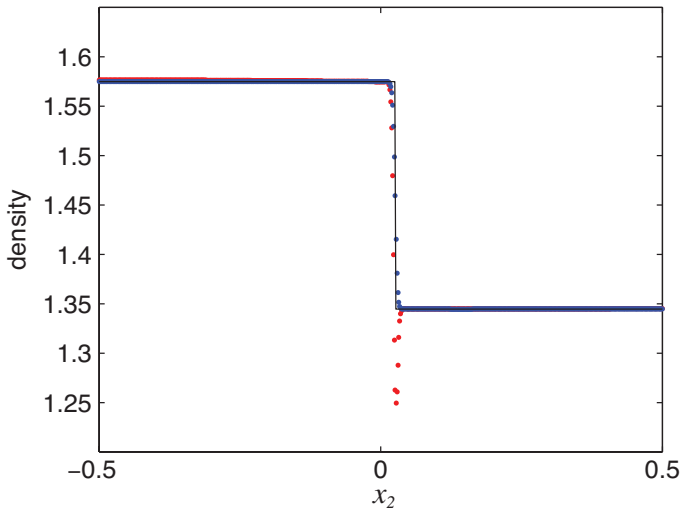

Fig. 14. Density along $x_1 = -0.25$ from the two-dimensional solution of the shock-interface problem at $t = 1$. The blue marks are from the solution of the energy-corrected scheme while the red marks are given by the uncorrected scheme. The exact solution in given by the black curve.

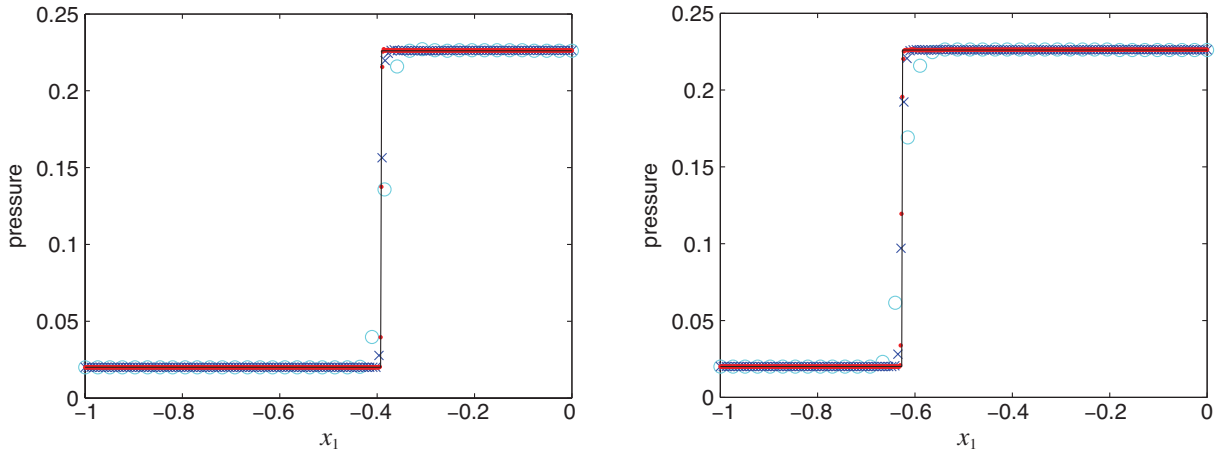

Fig. 15. Pressure along $x_2 = 0.5$ (left) and $x_2 = -0.5$ (right) from the two-dimensional solution of the shock-interface problem at $t = 1$. The numerical solutions for zero, one and two levels of AMR grids are shown (marks) along with the exact solution (black curves).

5.4 Planar Shock Interaction with Cylindrical Gas Bubbles

In this section we consider the interaction of a planar shock wave with cylindrical gas bubbles. The basic problem involves the interaction with an isolated bubble, and is motivated by experiments performed by Haas and Sturtevant [28], numerical calculations presented by Schwendeman [29], Quirk and Karni [3], and others. In the experiments, a relatively weak shock in air with shock Mach number equal to 1.22 impacts a cylindrical bubble filled with either helium or a refrigerant. For our numerical calculation of this problem, these materials are modeled as ideal gases with ratio of specific heats γ and specific heats (at constant volume) C_v taken from [3] and listed in Table 5. The air outside and the gas inside the bubble, either helium or refrigerant, are assumed to be in

temperature and pressure equilibrium prior to the impact of the shock, and the values for ρ_0 in Table 5 reflect this assumption. Ahead of the shock initially at $x_1 = 0.05$, the gas is at rest with uniform ambient pressure equal to 1.0. The state of the flow behind the shock is given by the usual shock conditions for air assuming the shock Mach number is 1.22. The cylindrical bubble has radius equal to 0.1 and is centered at $(x_1, x_2) = (0.2, 0.0)$. The base computational grid is given by (47) with $x_{1,c} = 0$, $x_{1,d} = 0.75$, $x_{2,d} = -x_{2,c} = 0.25$, $N_1 = 185$, and $N_2 = 123$. For our calculations, we use up to 2 AMR grid levels with refinement factor 4 on top of this base grid giving effective resolutions of $N_1 = 2960$ and $N_2 = 1968$. The bottom and top boundaries are modeled as solid (slip) walls and use a simple symmetry condition. The left boundary uses an inflow condition given by the initial state behind the shock, and the right boundary uses an outflow condition. All of these boundaries are at a sufficient distance from the bubble so that they do not play a role in the results shown.

	air	helium	refrigerant
γ	1.40	1.67	1.25
C_v	0.720	3.11	0.365
ρ_0	1.0	0.138	3.15

Table 5
Ideal equation of state parameters and ambient density for air, helium, and refrigerant. (The ambient density for air is normalized to one.)

Figure 16 shows numerical Schlieren images and shaded color contours of pressure for the interaction of a planar shock with a helium bubble at times $t = 0.02, 0.08, 0.16$, and 0.35. The images at $t = 0.02$ show the planar shock just before impact with the bubble. The shock is traveling from left to right in the figure and the bubble is stationary at this point. The Schlieren image on the left measures the magnitude of the gradient of density (see [30]) and shows the incident shock and material interface clearly. The right image shows the jump in pressure at the shock and pressure equilibrium at the material interface. At $t = 0.08$ the shock has impacted the bubble. Since the sound speed of the helium inside the bubble is much greater than the sound speed of air outside, the transmitted shock in the bubble has traveled well ahead of the incident shock and nearly reached the far boundary of the bubble. There is also a reflected shock generated from the initial interaction which travels away from the bubble in the flow behind the incident shock. At $t = 0.16$ the transmitted shock has reflected from the far boundary of the bubble with some transmission into the air. The reflected shock from this secondary interaction has traveled back through the bubble and into the air behind. This shock reflects back and forth inside the helium bubble several times before loosing enough strength so that it can no longer be seen. The final time, $t = 0.35$ shows the refracted shock well beyond the deformed bubble which is in the process of being divided. By this late time significant instability can be seen along the material interface in the form of roll ups and fingers. The plots show that the density and pressure are well behaved through the interface with no sign of the type of numerical errors discussed previously.

Since the sound speed of the helium inside the bubble is greater than the sound speed of the air outside, the helium-filled bubble acts as a divergent lens for the incident shock as discussed in [28]. The opposite case occurs for the refrigerant-filled bubble where the sound speed is lower inside the bubble. For this case, the bubble acts as a convergent lens as may be seen in the sequence of images shown in Figure 17. The left column in the figure shows numerical Schlieren images at times $t = 0.02$, 0.08, 0.16, and 0.35. At early times, we note that the transmitted shock lags behind the

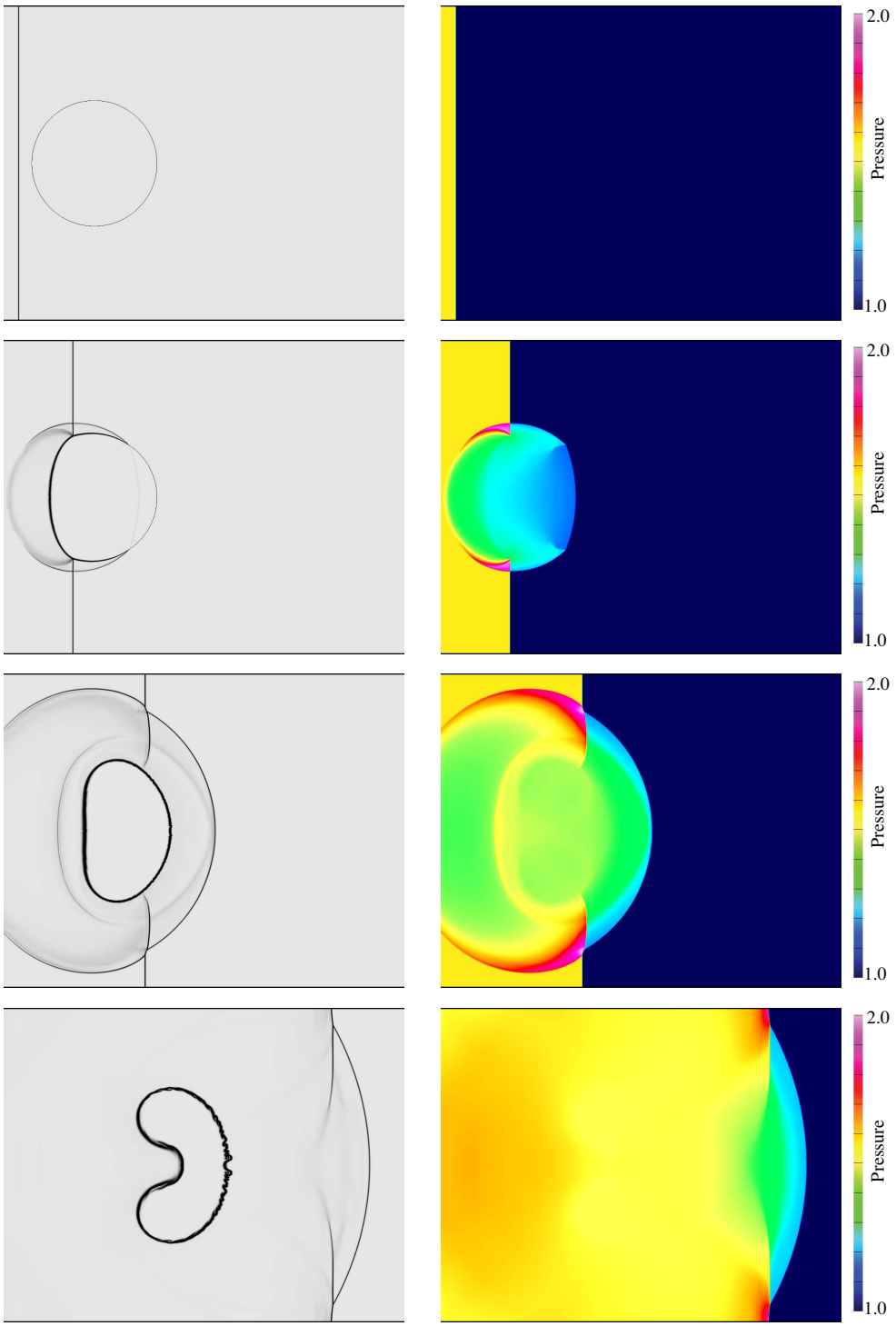

Fig. 16. Planar shock interaction with a helium-filled bubble at times $t = 0.02$, 0.08, 0.16, and 0.35 (top to bottom): numerical Schlieren images (left column) and shaded contours of pressure (right column).

incident shock and is concave forward. There is also faint shock reflected from the interface (see $t = 0.08$) which travels back into the flow. At $t = 0.16$ it has becomes clear that the shock will converge to some focus point. The final time in the sequence shows the shock diverging from that point of focus and roll ups along the unstable material interface. As before, we observe no numerical errors associated with the captured material interface, and good agreement with experimental [28] and numerical [3] results.

The numerical approach used to compute the behavior for an isolated bubble may be used to compute the flow for more general cases involving the interaction of a shock with several bubbles (or other curved inhomogeneities). For example, Figure 18 shows a configuration in which an incident planar shock (with shock Mach number equal to 1.22 in air as before) approaches a cluster of six cylindrical bubbles with radii ranging from 0.2 to 1.0 in the region $|x_1| \leq 5$ and $|x_2| \leq 5$. The subsequent behavior, shown in Figure 19, depends on the properties of the gas within the bubbles. The left column of Schlieren images in the figure shows the behavior for helium-filled bubbles at times $t = 2.0$, 4.0 and 6.0, while the behavior for refrigerant-filled bubbles is shown in the right column at the same three times. The computations are carried out on a base grid given by (47) with $x_{1,d} = x_{2,d} = -x_{1,c} = -x_{2,c} = 5$ and $N_1 = N_2 = 256$, and with two additional levels of AMR refinement using refinement factor 4.

The early behavior in which the shock first meets the leading bubbles is similar to that observed in the isolated bubble cases. At later times, the transmitted and reflected shocks from each bubble interact and the subsequent wave structure is complex. At the final time shown, the leading transmitted wave is generally convex forward for the helium case and concave forward for the refrigerant case indicating that the cluster of bubbles effectively acts as a divergent or convergent lens for the incident shock as might be expected. For the refrigerant case, each bubble generates a focusing event at various times near the rightmost boundary of each bubble. This focusing results in a pressure spike and a subsequent diverging shock similar to the isolated bubble case, but with several bubbles each focusing events can be either enhanced or suppressed by the complex interactions taking place. In our simulations, the largest pressure peak for the single bubble case occurs at $t = 0.263$ with a maximum pressure of 4.826. For the case of multiple bubbles the focusing event for the bubble at the lower right occurs at $t = 5.78$ with a maximum pressure of 5.720 while the focusing event for the bubble at the upper right occurs at $t = 4.82$ with a maximum pressure of 3.710. These focusing events are shown in Figure 20.

5.5 Cylindrical Vessel

In order to demonstrate the capability of the method for overlapping grids with AMR, we present a final computation of a multi-material flow in a rigid cylindrical vessel. For this problem, the vessel is filled with two ideal gases separated by a material interface which is planar initially. The vessel is then impulsively driven normal to the interface causing a curved shock to form along the compressive portion of the boundary and a rarefaction to form along the opposing portion of the boundary. (For the purposes of computation, it is simpler to keep the vessel fixed and consider a flow with an initial uniform velocity.) The shock propagates away from the boundary and interacts with the material interface resulting a complex flow which we describe below.

To set the conditions of the problem, we assume that the cylindrical vessel has radius 0.8 and

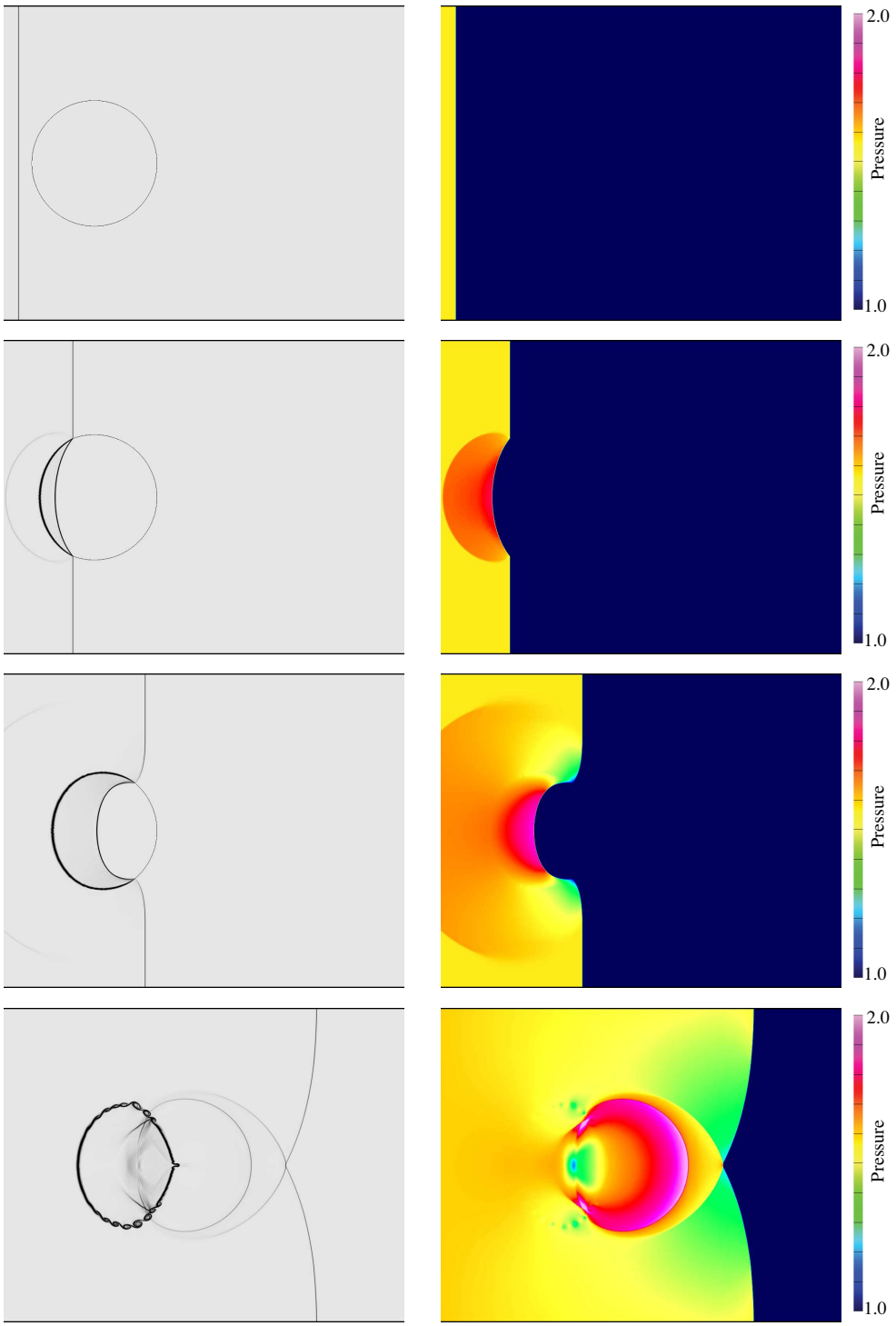

Fig. 17. Planar shock interaction with a refrigerant-filled bubble at times $t = 0.02$, 0.08, 0.16, and 0.35 (top to bottom): numerical Schlieren images (left column) and shaded contours of pressure (right column).

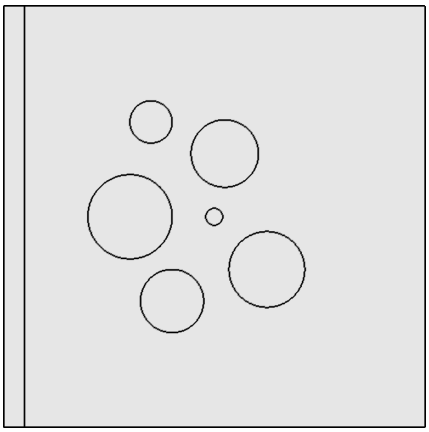

Fig. 18. Numerical Schlieren images of a planar shock in air impacting a cluster of cylindrical bubbles: initial configuration.

is centered at the origin, $x_1 = x_2 = 0$. The material interface is located at $x_1 = 0$ initially and separates air for $x_1 < 0$ and helium for $x_1 > 0$. The parameters for each gas are taken from Table 5 with the initial pressure set to 1.0 throughout the domain. We attach ourselves to the frame of the vessel and take the components (u_1, u_2) of the fluid velocity to be $(-1, 0)$ initially throughout the domain. Numerical solutions are computed using a (base-level) overlapping grid consisting of a background Cartesian grid and an annular boundary-fitted grid. The Cartesian grid is given by (47) with $x_{1,d} = x_{2,d} = -x_{1,c} = -x_{2,c} = 0.8$ and $N_1 = N_2 = 4N$, and the annular grid is given by (48) with $r_c = 0.8 - 6.4/(4N)$, $r_d = 0.8$, $\theta_c = 0$, $\theta_d = 2\pi$, $N_r = 5$ and $N_\theta = 12N$. The integer N is used to vary the resolution of the base-level grids. For this grid construction the number of grid lines in the radial direction of the annular grid is fixed while the width of the annular grid decreases with increasing N. This is done so that the bulk of the grid points lie on the Cartesian grid as N increases.

Figure 21 shows the behavior of the solution at times $t = 0.25$, 0.5, 0.75 and 1.0. The calculations shown in this figure use $N = 40$ for the base-level grids and two additional levels of refinement grids with refinement factor equal to 4. The basic evolution of the solution is dominated by the shock which forms on the left and propagates to the right towards the material interface. The shock is seen as a nearly semi-circular wave in the top pair of plots ($t = 0.25$) while the interface is seen as an approximately vertical line near the center of the domain. The leading edge of the expansion generated from the boundary of the cylindrical vessel on the right has propagated to the left and through the material interface. It is seen in the plots at $t = 0.25$ as two nearly radial lines emerging from the center of the vessel. By $t = 0.5$ the shock has already focused, and its central portion has collided with the interface and passed through it into the helium on the right. Once in the helium, the shock diverges rapidly and reflects off the boundary on the right. The flow behind the diverging shock now drives the material interface to the right in the central portion of the vessel. The plots at $t = 0.75$ show the curved reflected shock which travels to the left. There is also a small high-pressure region in the air on the left which is a remnant of the earlier focussing event. The curved reflected shock, in turn, passes back through the interface into the air and focusses as seen in the final pair of plots at $t = 1.0$. The material interface has rolled up as result of a Richtmyer-Meshkov instability caused by the passage of the various shocks through the interface.

In order to investigate the effect of the grid overlap on the numerical solution, we compare the solution shown in Figure 21 with a solution computed using a different base-level overlapping grid.

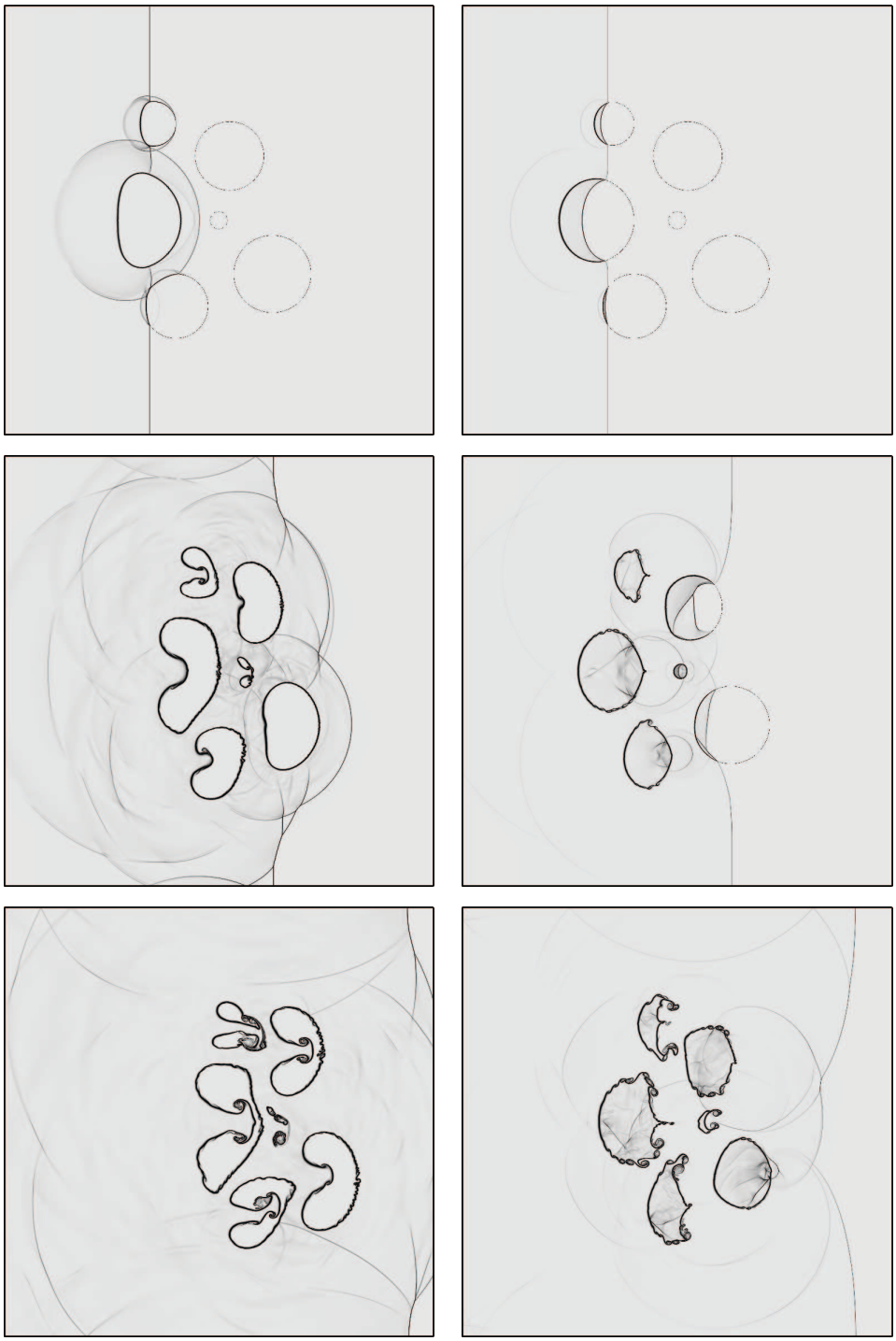

Fig. 19. Numerical Schlieren images of a planar incident shock in air impacting a cluster of cylindrical bubbles: helium-filled bubbles (left column) and refrigerant-filled bubbles (right column). The times from top to bottom are $t = 2.0$, 4.0 and 6.0.

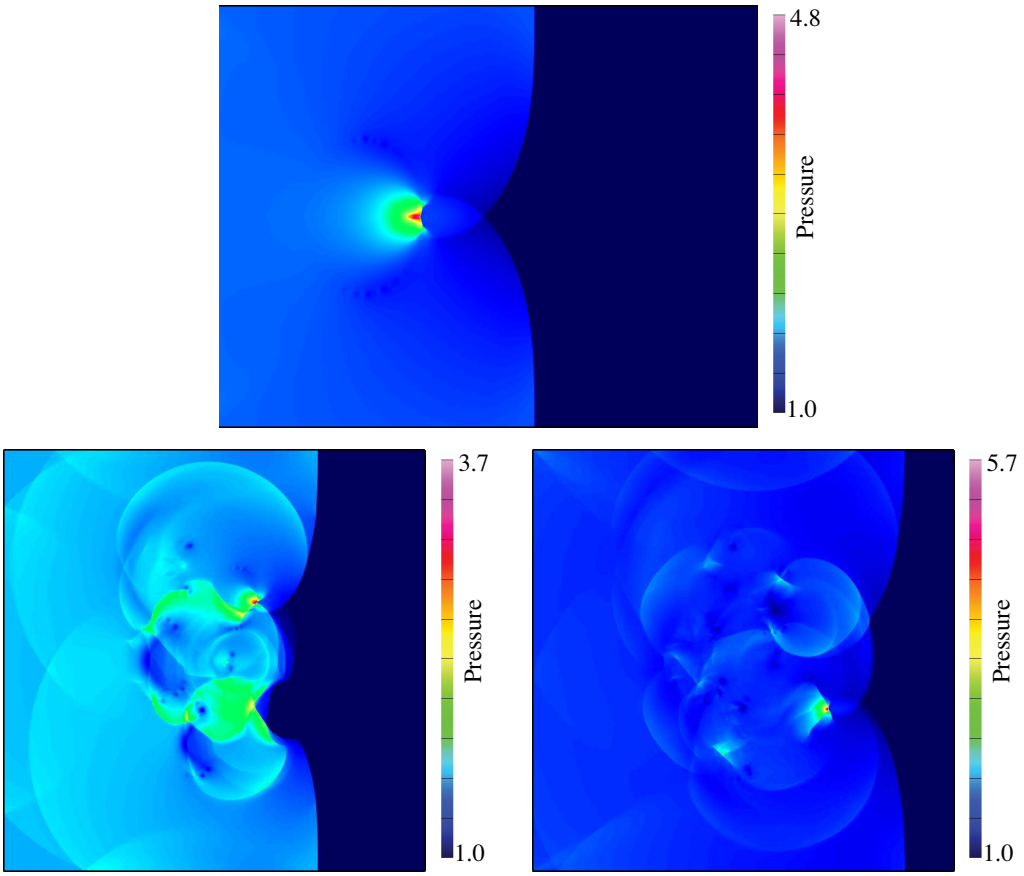

Fig. 20. Shaded contours of pressure at shock focus for a single refrigerant-filled bubble (top, $t = 0.263$) and for a collection of refrigerant-filled bubbles (bottom left, $t = 4.82$ and bottom right, $t = 5.78$). The shock-bubble interactions for the collection of bubbles can serve to either suppress (bottom left) or enhance (bottom right) the peak pressure attained at the moment of shock focusing.

The base-level grids used for the comparison are shown in Figure 22. The grid on the top right in the figure was used for the previous calculation and its grid overlap is very close to the boundary of the cylindrical vessel. The grid on the bottom right has a much thicker annular component grid and its overlap occurs near a radius equal to 0.4. (This latter grid was used for the convergence study in Section 5.1.) Both base-level grids have approximately the same grid spacings and numerical solutions are computed for both grids with two levels of refinement grids as before. Corresponding numerical Schlieren images of the solutions at $t = 1.0$ are displayed in the figure on the left. We observe that the overall behavior of the shocks, contacts and material interface are essentially the same for both calculations. The main difference appears in the fine-scale structure of the instability that occurs along the material interface. This difference is attributed to numerical perturbations from both the grid overlap and from the roughly planar material interface traveling obliquely to the annular section for a larger portion of the domain in the case on the right where the annular grid is thicker.

As a final calculation we compare numerical solutions at $t = 1.0$ for increasing grid resolution. The base-level grid used for this study is that shown on the top right in Figure 22 with $N = 10$, 20 and 40, and with two refinement levels for each case. Figure 23 shows Schlieren images at $t = 1.0$

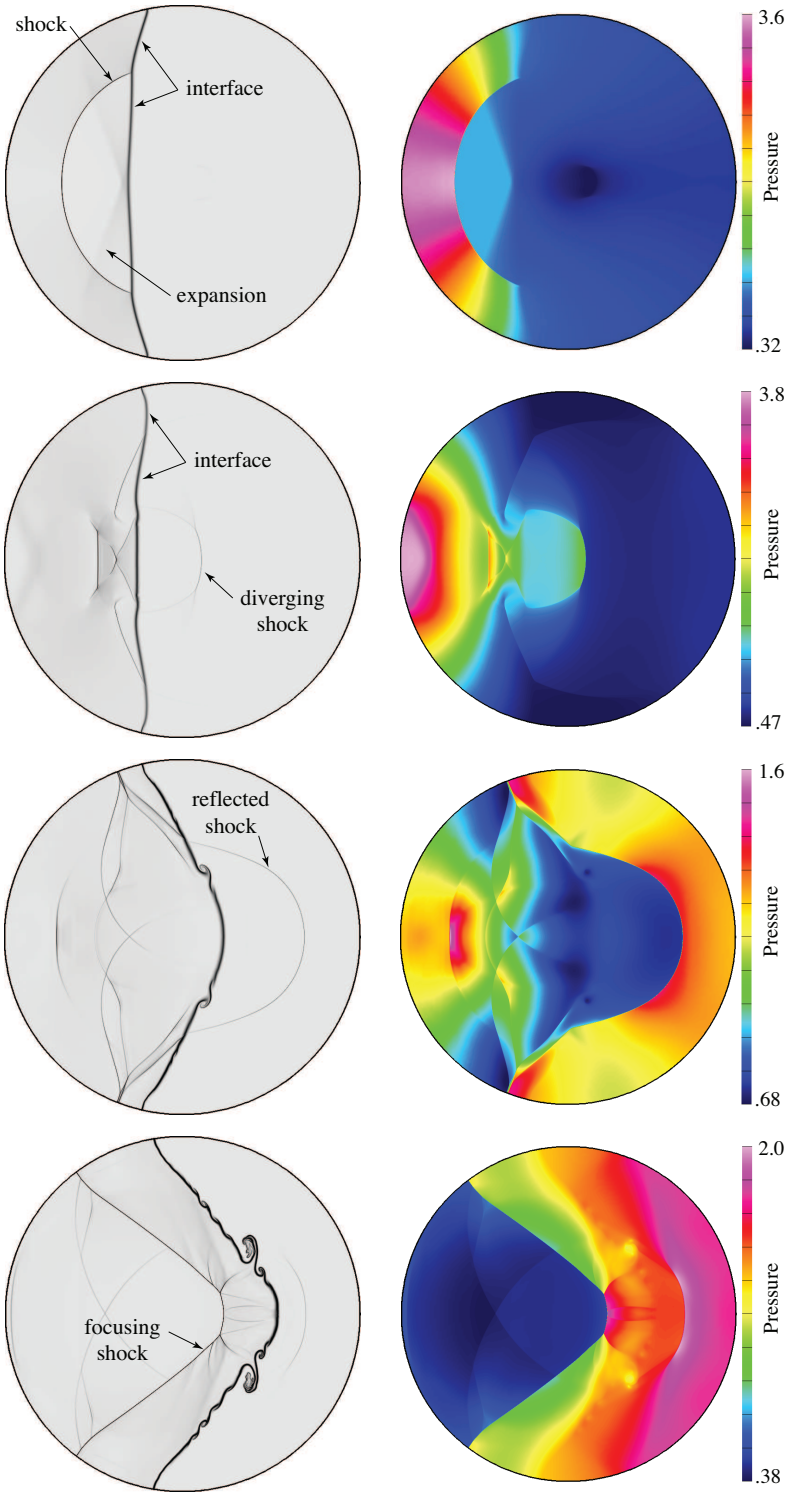

Fig. 21. Numerical Schlieren images (left) and shaded contours of pressure (right) for an impulsively driven cylinder containing a material interface separating air and helium. Solutions from top to bottom are at times $t = 0.25$, 0.5, 0.75, and 1.0.

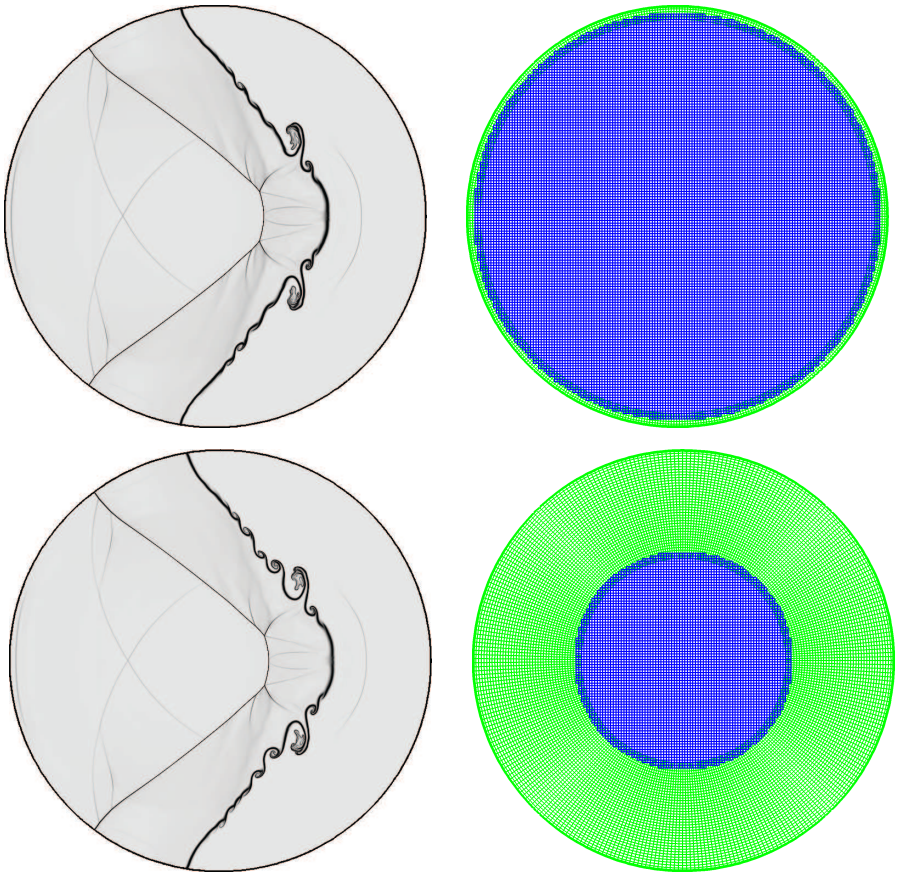

Fig. 22. Base-level grids (right) and numerical Schlieren images at $t = 1.0$ (left) for an impulsively moved cylindrical vessel.

from these three calculations along with the structure of the grid refinement. As the resolution increases, the captured shocks and material interface sharpen, as expected, and we note an increase in the amount of fine-scale structure along the unstable material interface. For the calculations using the coarser base-level grids, the error estimator flags all points on the base-level so that the whole domain is covered by refinement grids on the first level. As the base-level grids refine, the refinement-grid structure increasingly localizes the fine-scale structures in the solution so that they are captured well at the finest resolution.

6 Conclusions

We have described a numerical method for the solution of high-speed multi-material flows. The method is an extension of a standard shock-capturing scheme with the addition of a numerical source term at the level of the truncation error designed to suppress numerical errors occurring as a result of a captured material interface. The numerical source is computed using an auxiliary set of special Riemann problems which allows for general equations of state to be used. These Riemann problems involve uniform-pressure-velocity flow and thus the corresponding Godunov flux is an upwind flux which is computed easily. This allows efficient computation with the result that the overall computational cost of the method is not significantly more than the original shock-capturing

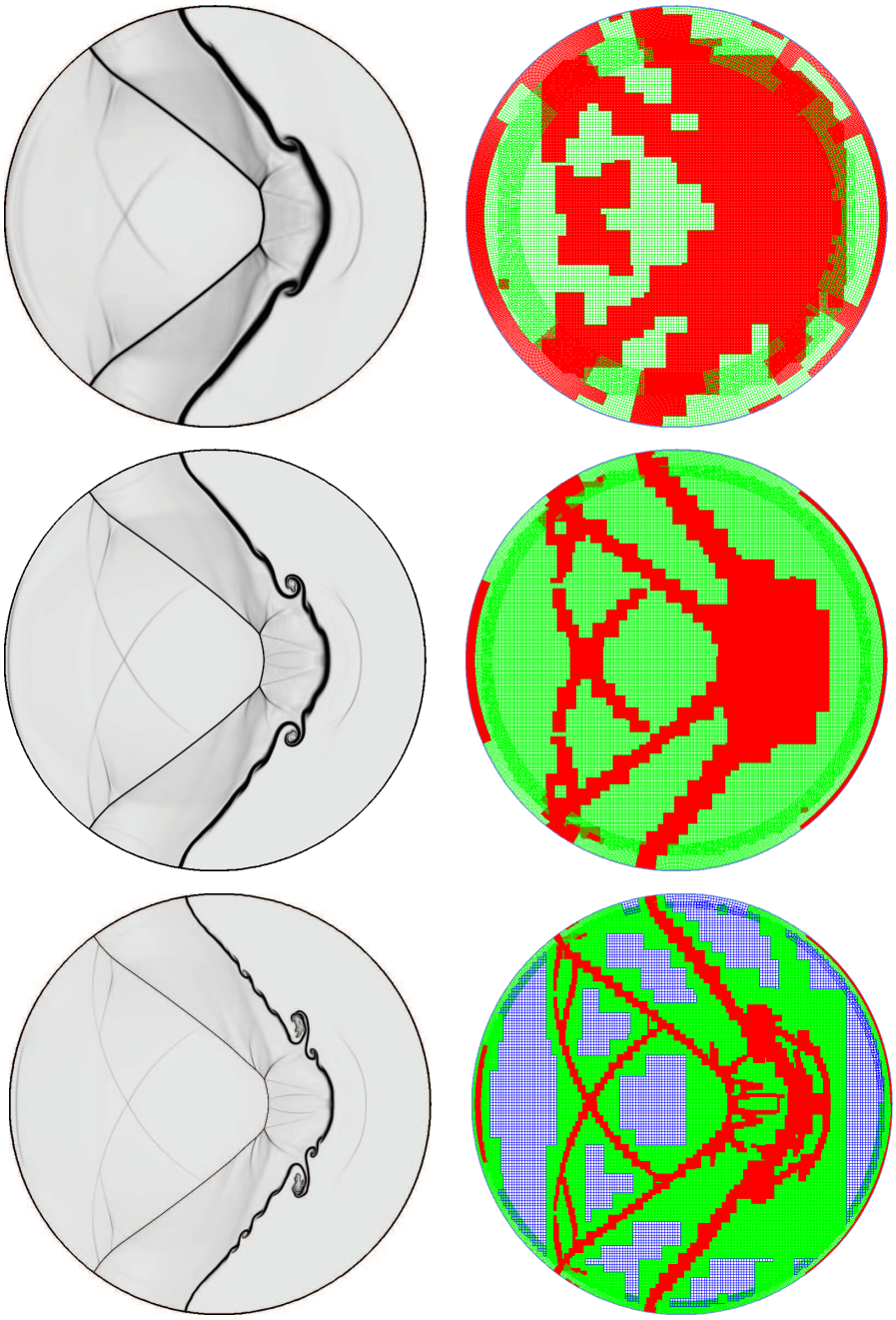

Fig. 23. Numerical Schlieren images at $t = 1.0$ (left) and the AMR grid structure (right) for an impulsively moved cylindrical vessel. For the grids, the base grid is colored blue, the first level of AMR refinement is green, and the second level of AMR refinement is red. The effective grid spacings from top to bottom are $0025, 0.00125$, and 0.000625.

scheme. The numerical method is applied to two-dimensional flow using overlapping grids. Complex geometries can be described using these overlapping grids while maintaining computational efficiency because the bulk of the grid points lie on Cartesian component grids. Adaptive mesh refinement is used to capture fine structures in the flow such as shocks, contact, and material interfaces. While the method can accommodate any mixture equation of state, we have focussed our attention on an equation of state constructed assuming JWL equations of state for each component

of the mixture. This form also includes a mixture of ideal gases as a special case.

A series of test problems have been discussed in order to verify the accuracy of new numerical method. Convergence studies on smooth flows were performed using the method of analytic solutions. These calculations were carried out on a sequence of Cartesian grids and a sequence of overlapping grids with increasing grid resolution. A comparison was made between the numerical solution and the exact solution, and second-order convergence of the method was shown for smooth flow. The behavior of the method for flows involving the interaction of the interface and a shock was examined using both one-dimensional and two-dimensional flow where exact solutions are known. The one-dimensional problem investigated a shock impacting a material interface in several ways. In one setup, the interface moved relative to the grid and thus became smeared over a few grid cells prior to collision with the shock. In another setup, the interface was stationary relative to the grid and thus remained sharp prior to collision. Finally, in a third setup, an overlapping grid was used and the interface was positioned on the overlap prior to collision with the shock. All three cases showed good agreement with the exact solution with no numerical oscillations near the material interface that arise using standard shock-capturing methods. An exact solution for a non-trivial two-dimensional flow was constructed using shock polars assuming a two-component mixture described by JWL equations of state. Again, the numerical method was shown to give accurate results.

Two additional problems in which exact solutions are not available were discussed in order to further demonstrate the capabilities of the method. The first involved an incident planar shock in air impacting an isolated cylindrical bubble or a collection of several bubbles filled with either helium or refrigerant. For the case of an isolated bubble, the problem has been extensively studied both numerically and experimentally, and our calculations are found to be in good agreement with those previous results. We introduce an additional level of complexity by performing a computation of a collection of cylindrical bubbles of varying sizes. For the refrigerant case, it is found that the interaction of the incident shock and the leading bubbles has a significant effect on the interaction of the disturbed shock with later bubbles resulting in shock-focusing pressure rise to be amplified for some bubbles while diminished for others. The second problem is one of an impulsively driven cylinder containing a material interface and is meant to highlight the application of the method for overlapping grids. Calculations are carried out on two overlapping grids with difference overlap position. The results are found to be in good agreement with only slight differences in the behavior of the unstable material interface. A further grid-refinement study showed the convergence of the bulk of flow features and the emergence of a Richtmyer-Meshkov instabilities as the grid became increasingly refined.

We have shown how a standard shock-capturing method such as Godunov's method may be modified to effectively and efficiently compute multi-material flows. Our focus has been on inert flows, but our numerical approach may be extended to treat reactive flow. This extension is in progress.

Acknowledgements

The authors thanks Tariq Aslam and John Bdzil for helpful discussions during the development of this work. In particular, Tariq Aslam suggested the form of the two-dimensional shock-interface test case discussed in Section 5.3.

References

[1] S. Karni, Viscous shock profiles and primitive formulations, SIAM J. Numer. Anal. 29 (6) (1992) 1592–1609.

[2] S. Karni, Multicomponent flow calculations by a consistent primitive algorithm, J. Comput. Phys. 112 (1994) 31–43.

[3] J. J. Quirk, S. Karni, On the dynamics of a shock-bubble interaction, J. Fluid Mech. 318 (1996) 129–163.

[4] R. Abgrall, How to prevent pressure oscillations in mulicomponent flow calculations: A quasi conservative approach, J. Comput. Phys. 125 (1996) 150–160.

[5] R. Saurel, R. Abgrall, A simple method for compressible multifluid flows, SIAM J. Sci. Comput. 21 (3) (1999) 1115–1145.

[6] P. Jenny, B. Müller, H. Thomann, correction of conservative Euler solvers for gas mixtures, J. Comput. Phys. 132 (1997) 91–107.

[7] R. P. Fedkiw, T. Aslam, B. Merriman, S. Osher, A non-oscillatory Eulerian approach to interfaces in multimaterial flows (the ghost fluid method), J. Comput. Phys. 152 (1999) 457–492.

[8] R. Fedkiw, T. Aslam, S. Xu, The ghost fluid method for deflagration and detonation discontinuities, J. Comput. Phys. 154 (1999) 393.

[9] S. Xu, T. Aslam, D. Stewart, High resolution numerical simulation of ideal and non-ideal compressible reacing flows with embedded internal boundaries, Combust. Theory Modelling 1 (1997) 113–142.

[10] C. Hirt, A. Amsden, J. Cook, An arbitrary Lagrangian-Eulerian computing method for all speed flows, J. Comput. Phys. 14 (3) (1974) 227–253.

[11] R. Anderson, N. Elliott, R. Pember, A dynamically adaptive arbitrary Lagrangian-Eulerian method for solution of the Euler equations, Tech. Rep. Research Report UCRL-JC-151904, Lawrence Livermore Laboratory National Laboratory (2003).

[12] K.-M. Shyue, A wave-propagation based volume tracking method for compressible multicomponent flow in two space dimensions, J. Comput. Phys. (2006) in press.

[13] H. S. Udaykumar, L. Tran, D. M. Belk, K. J. Vanden, An eulerian method for computation of multimaterial impact with eno shock-capturing and sharp interfaces, J. Comput. Phys. 186 (2003) 136–177.

[14] R. Abgrall, S. Karni, Computations of compressible multifluids, J. Comput. Phys. 169 (2001) 594–623.

[15] S. K. Godunov, Difference methods for the numerical calculation of the equations of fluid dynamics, Mat. Sb. 47 (1959) 271–306.

[16] G. Cheshire, W. Henshaw, Composite overlapping meshes for the solution of partial differential equations, J. Comput. Phys. 90 (1990) 1–64.

[17] M. J. Berger, J. Oliger, Adaptive mesh refinemenr for hyperbolic partial differential equations, J. Comp. Phys. 53 (1984) 484–512.

[18] W. D. Henshaw, D. W. Schwendeman, An adaptive numerical scheme for high-speed reactive flow on overlapping grids, J. Comput. Phys. 191 (2) (2003) 420–447.

[19] W. Fickett, W. C. Davis, Detonation, University of California Press, Berkeley, 1979.

[20] B. M. Dobratz, Properties of chemical explosives and explosive simulants, Tech. Rep. LLNL UCRL-51319, Lawrence Livermore Laboratory National Laboratory (July 1974).

[21] E. L. Lee, C. M. Tarver, Phenomenological model of shock initiation in hetrogeneous explosives, Phys. Fluids 23 (12) (1980) 2362–2372.

[22] C. M. Tarver, J. O. Hallquist, Modeling two-dimensional shock initiation and detonation wave phenomenon in PBX-9404 and LX-17, The Seventh Symposium (International) on Detonation (1981) 488–497.

[23] C. M. Tarver, J. O. Hallquist, L. M. Erickson, Modeling short-pulse duration shock initiation of solid explosives, The Eighth Symposium (International) on Detonation (1985) 951–960.

[24] R. J. LeVeque, Numerical Methods for Conservation Laws, Birkhauser, Basel, 1992.

[25] P. Glaister, An approximate linearised riemann solver for euler equations for real gases, J. Comput. Phys. 74 (1988) 382–408.

[26] J. M. Powers, Two-phase viscous modeling of compaction in granular explosives, Phys. Fluids 16 (8) (2004) 2975–2990.

[27] T. D. Aslam, J. B. Bdzil, Numerical and theoretical investigations on detonation-inert confinement interactions, in: The Twelfth Symposium (International) on Detonation, 2002, pp. 483–488.

[28] J. Haas, B. Sturtevant, Interaction of weak shock waves with cylindrical and spherical gas inhomogeneities, J. Fluid Mech. 181 (1987) 41–76.

[29] D. W. Schwendeman, Numerical shock propagation in non-uniform media, J. Fluid Mech. 188 (1988) 383–410.

[30] W. D. Henshaw, D. W. Schwendeman, Moving overlapping grids with adaptive mesh refinement for high-speed flow, J. Comput. Phys. (to appear).